Газогидраты и Bottom Simulating Reflectors (BSRs)

А.М. Никишин

Газогидраты, общие вопросы

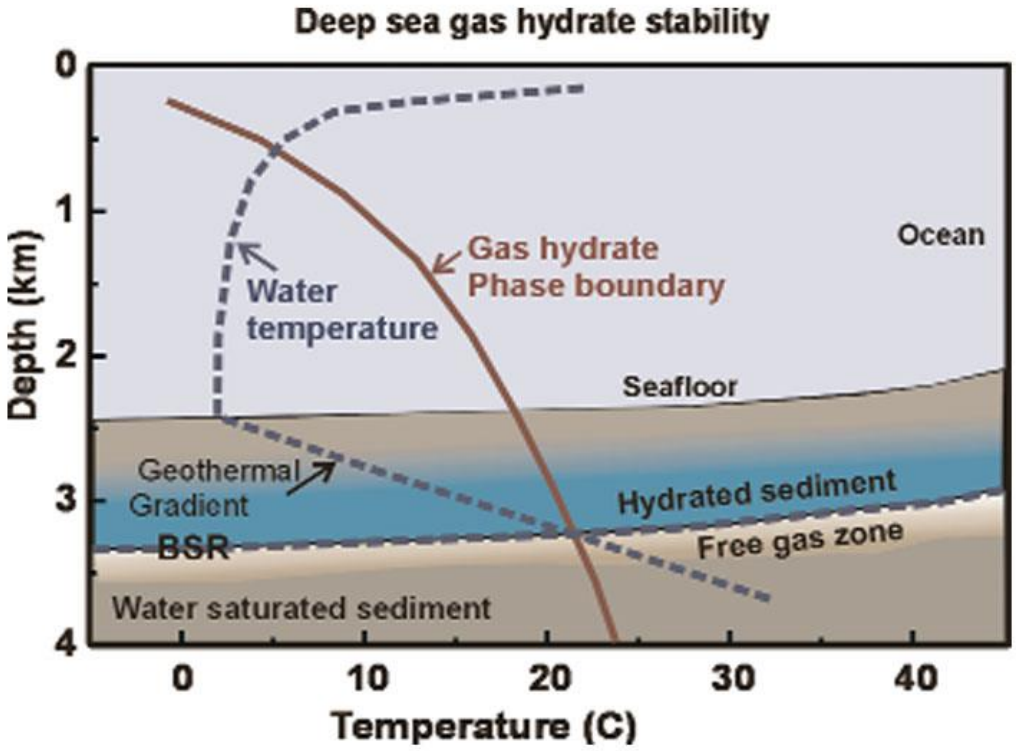
Deep sea gas hydrate stability
Depth (km)
Temperature (C)
Ocean
Seafloor
Water temperature
Gas hydrate Phase boundary
Geothermal Gradient
BSR
Hydrated sediment
Free gas zone
Water saturated sediment

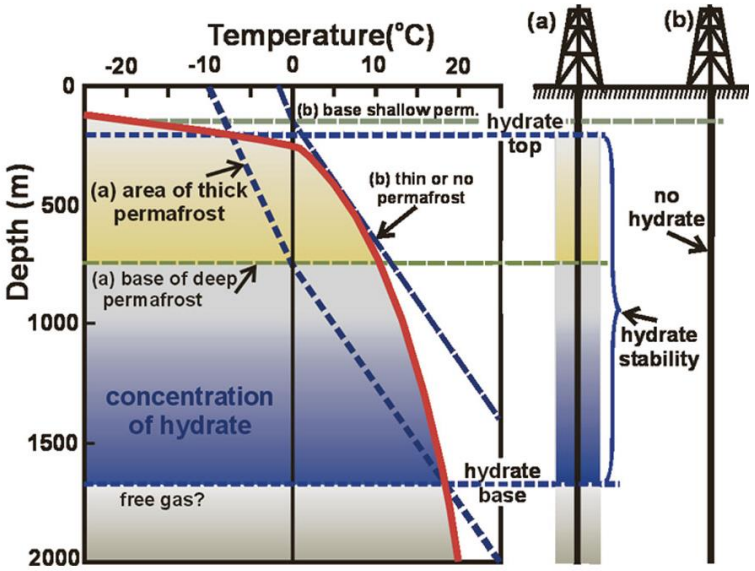
Temperature(°C)
Depth (m)
(a)
(b)
(b) base shallow perm.
hydrate top
(a) area of thick permafrost
(b) thin or no permafrost
no hydrate
(a) base of deep permafrost
hydrate stability
concentration of hydrate
hydrate base
free gas?

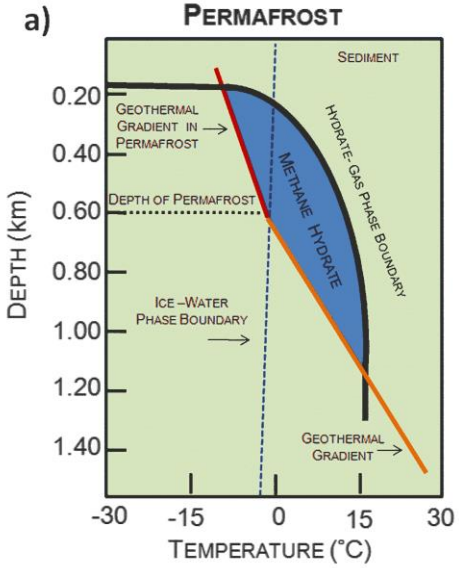
a)
PERMAFROST
SEDIMENT
GEOTHERMAL GRADIENT IN PERMAFROST
DEPTH OF PERMAFROST
METHANE HYDRATE
HYDRATE-GAS PHASE BOUNDARY
ICE–WATER PHASE BOUNDARY
GEOTHERMAL GRADIENT
DEPTH (km)
TEMPERATURE (°C)

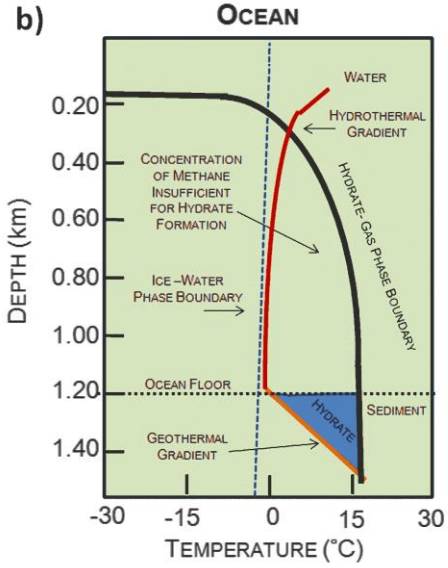
b)
OCEAN
WATER
HYDROTHERMAL GRADIENT
CONCENTRATION OF METHANE INSUFFICIENT FOR HYDRATE FORMATION
HYDRATE-GAS PHASE BOUNDARY
ICE–WATER PHASE BOUNDARY
OCEAN FLOOR
HYDRATE
SEDIMENT
GEOTHERMAL GRADIENT
DEPTH (km)
TEMPERATURE (°C)

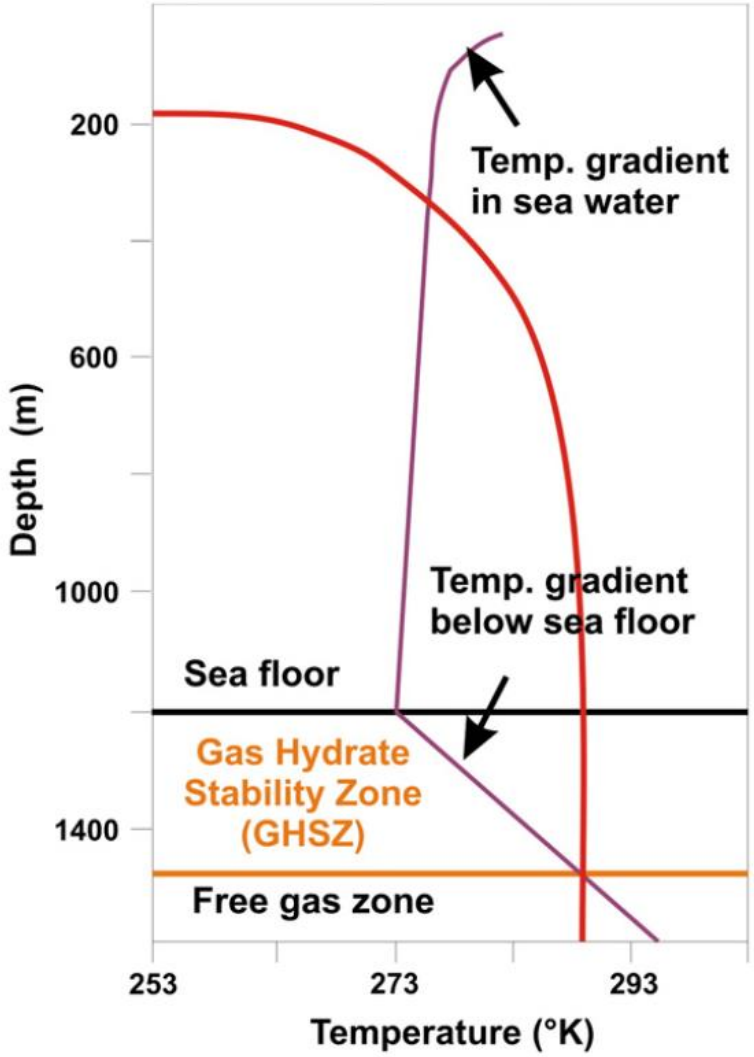

Fig. 1. A) Methane hydrate phases; B) typical occurrence of the gas hydrate stability zone on continental margins. A water depth of 1200 m is assumed. The viola purple line represents the geothermal curve, while the red line is the gas hydrate stability curve. The orange line marks the depth of the base of gas hydrate stability zone.

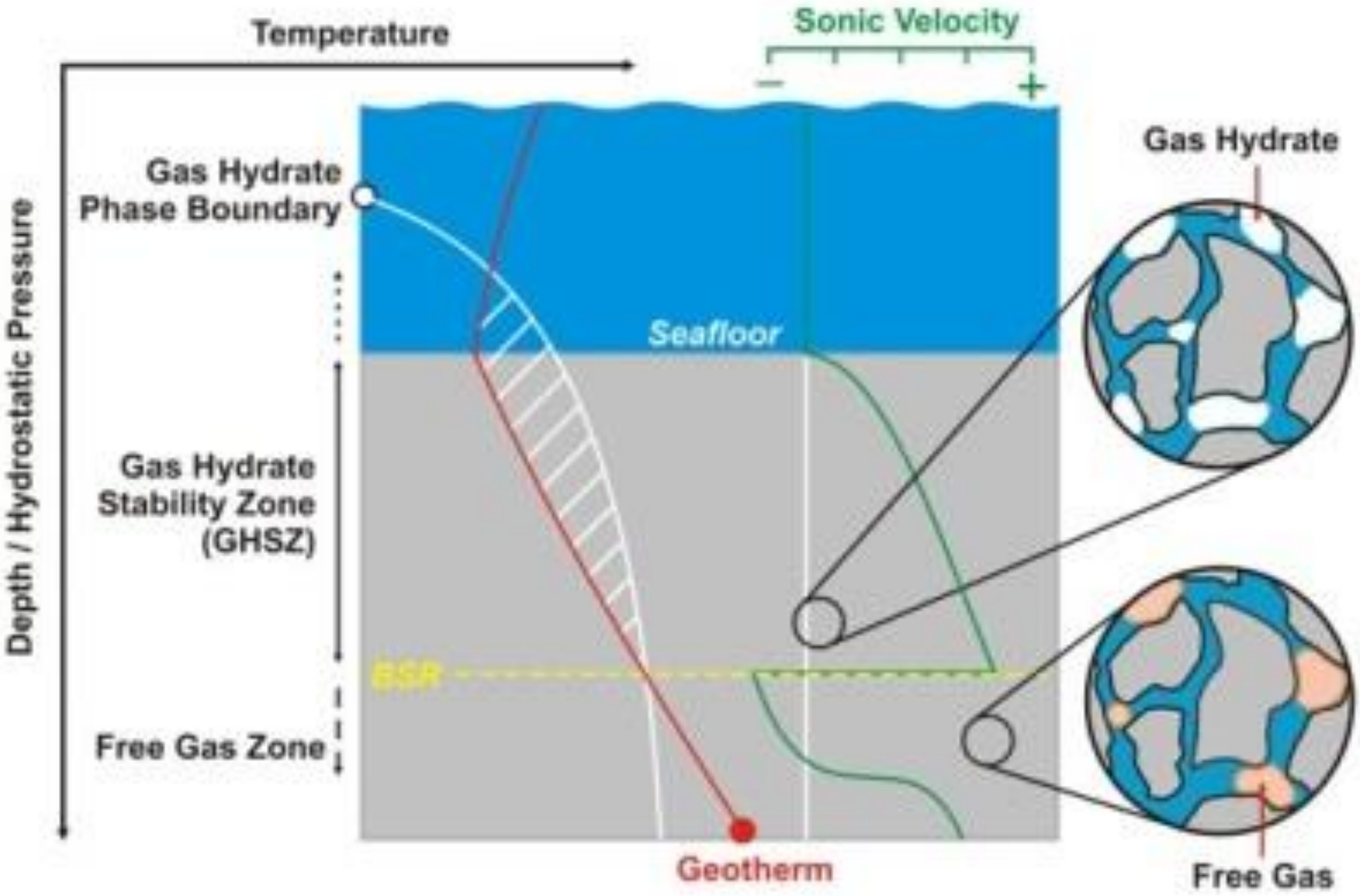
Temperature
Sonic Velocity
−
+
Depth / Hydrostatic Pressure
Gas Hydrate
Phase Boundary
Seafloor
Gas Hydrate
Stability Zone
(GHSZ)
BSR
Free Gas Zone
Geotherm
Gas Hydrate
Free Gas

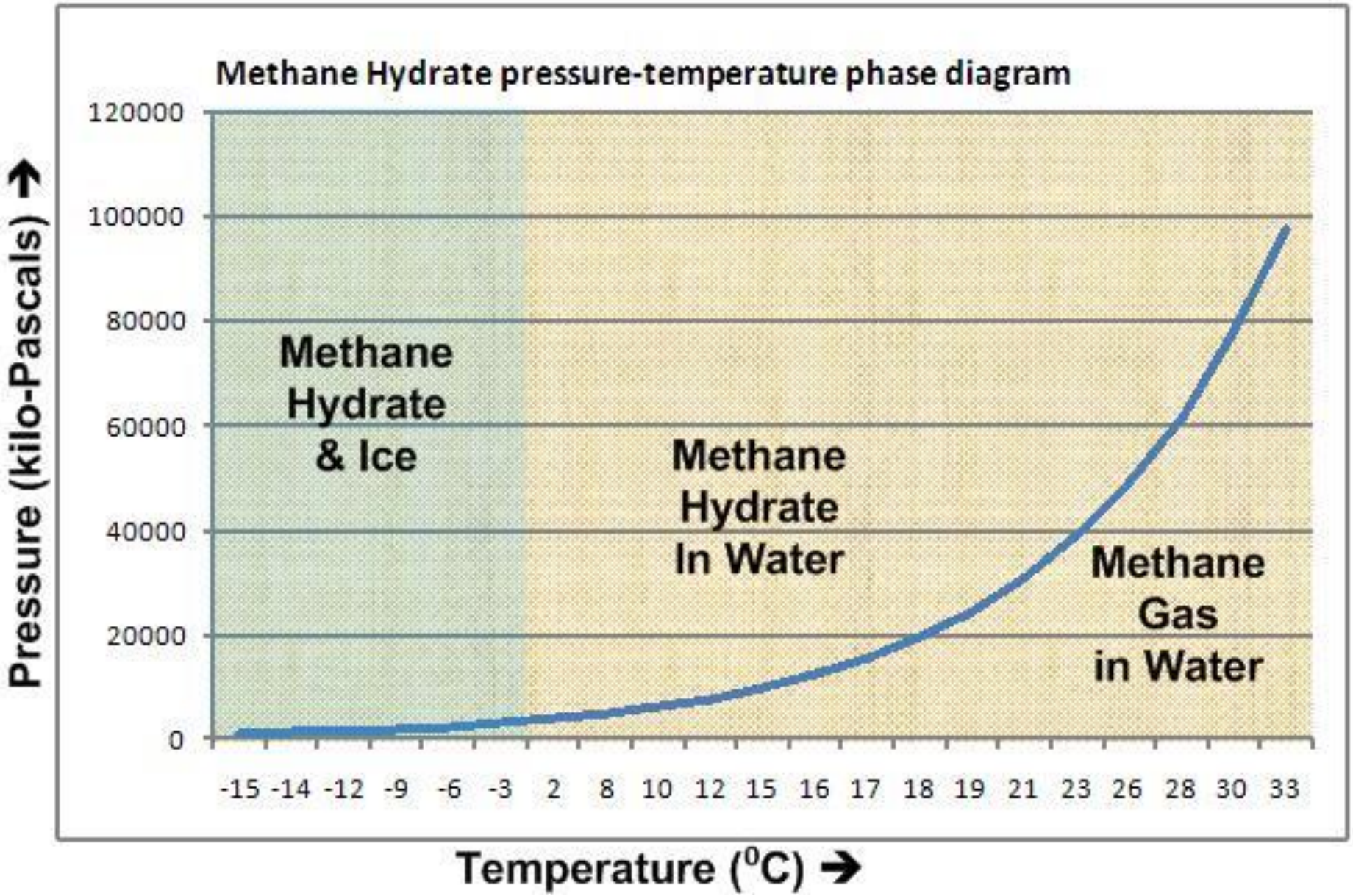
Methane Hydrate pressure-temperature phase diagram
120000
100000
80000
60000
40000
20000
0
Pressure (kilo-Pascals) →
Methane Hydrate & Ice
Methane Hydrate In Water
Methane Gas in Water
-15 -14 -12 -9 -6 -3 2 8 10 12 15 16 17 18 19 21 23 26 28 30 33
Temperature (⁰C) →

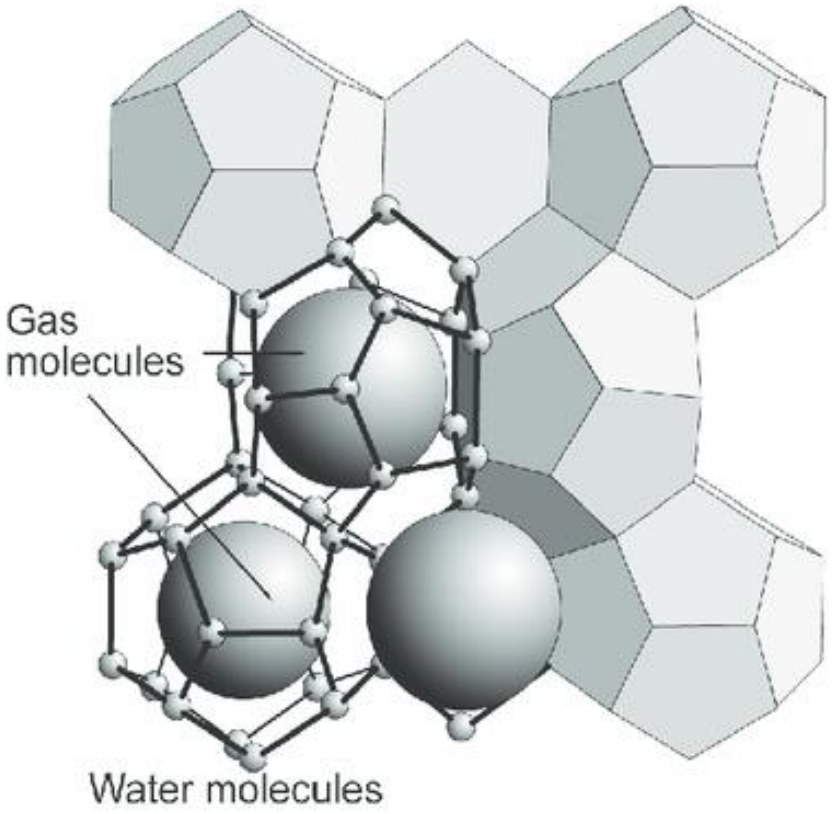
Gas
molecules
Water molecules

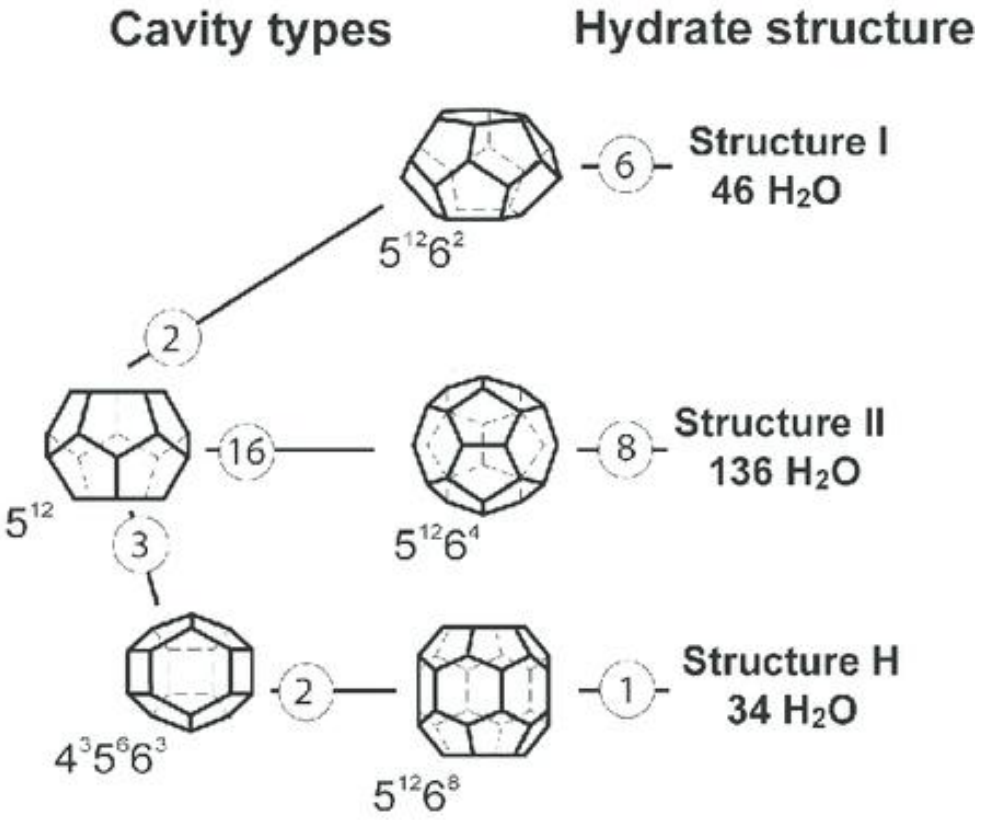
Cavity types
Hydrate structure
6
Structure I
46 H2O
5^12 6^2
2
16
8
Structure II
136 H2O
5^12
5^12 6^4
3
2
1
Structure H
34 H2O
4^3 5^6 6^3
5^12 6^8

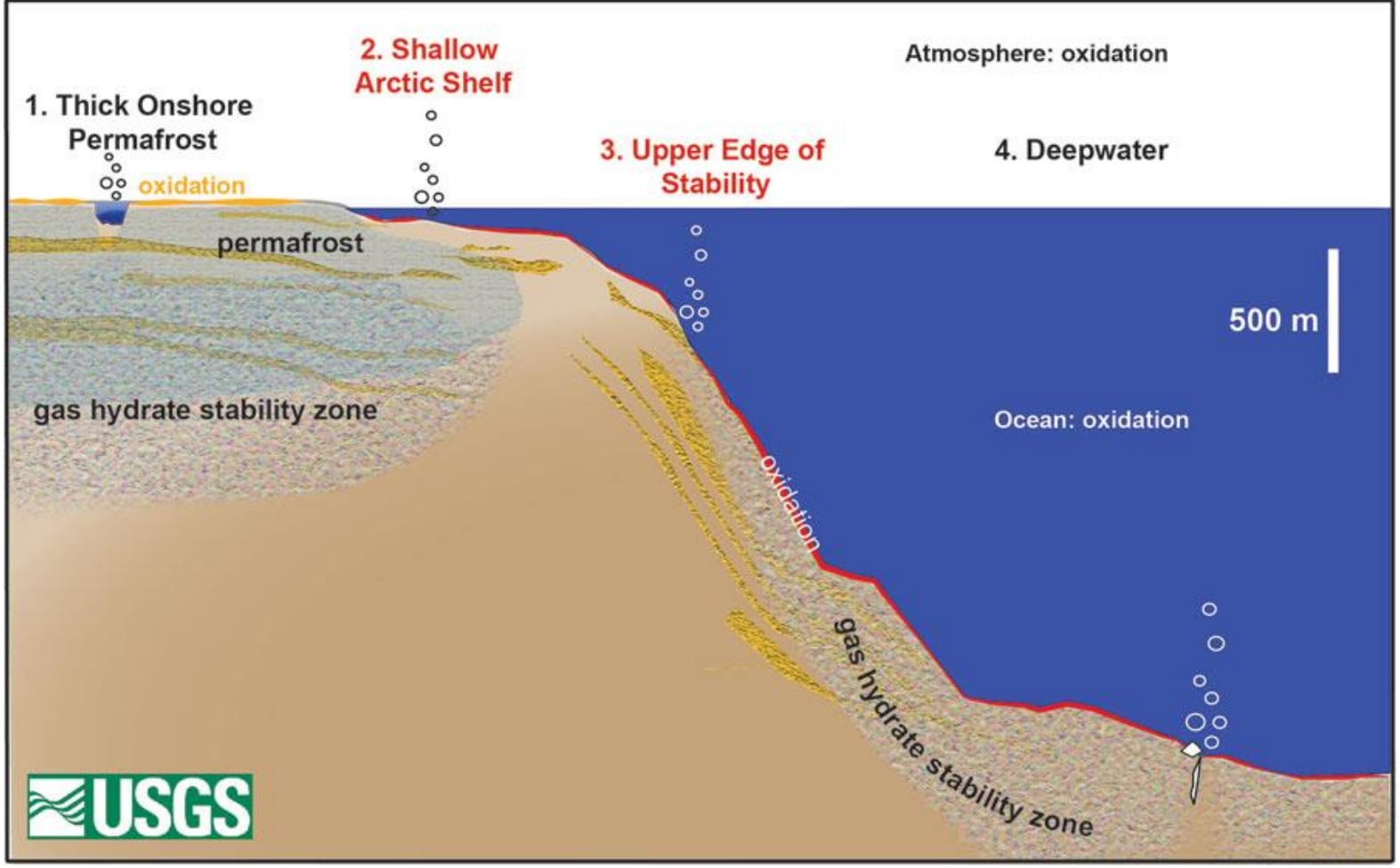
1. Thick Onshore Permafrost
2. Shallow Arctic Shelf
3. Upper Edge of Stability
4. Deepwater
Atmosphere: oxidation
oxidation
permafrost
gas hydrate stability zone
500 m
Ocean: oxidation
oxidation
gas hydrate stability zone
USGS

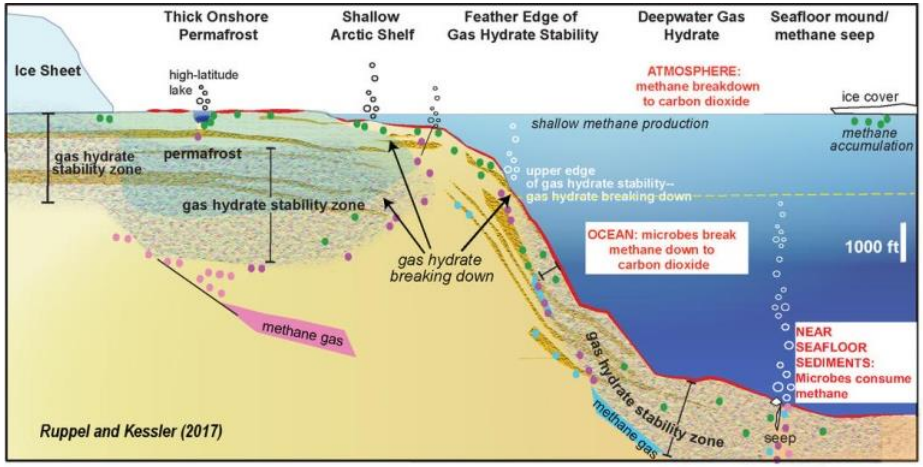
Thick Onshore Permafrost
Shallow Arctic Shelf
Feather Edge of Gas Hydrate Stability
Deepwater Gas Hydrate
Seafloor mound/ methane seep
Ice Sheet
high-latitude lake
ATMOSPHERE: methane breakdown to carbon dioxide
ice cover
shallow methane production
methane accumulation
gas hydrate stability zone
permafrost
upper edge of gas hydrate stability-- gas hydrate breaking down
gas hydrate stability zone
OCEAN: microbes break methane down to carbon dioxide
1000 ft
gas hydrate breaking down
methane gas
NEAR SEAFLOOR SEDIMENTS: Microbes consume methane
gas hydrate stability zone
methane gas
seep
Ruppel and Kessler (2017)

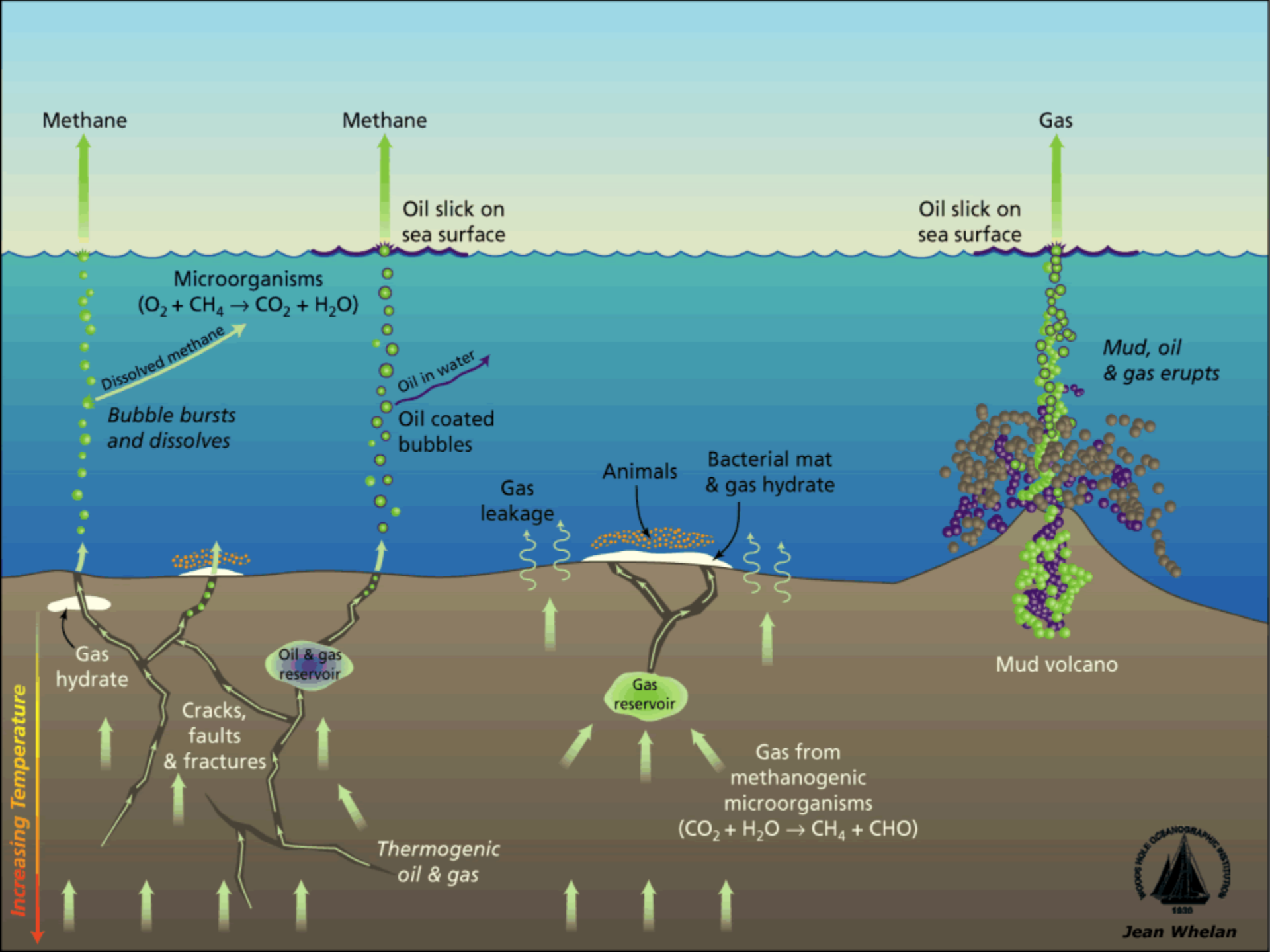
Methane
Methane
Gas
Oil slick on sea surface
Oil slick on sea surface
Microorganisms
$(O_2 + CH_4 \rightarrow CO_2 + H_2O)$
Dissolved methane
Oil in water
Bubble bursts and dissolves
Oil coated bubbles
Mud, oil & gas erupts
Animals
Bacterial mat & gas hydrate
Gas leakage
Gas hydrate
Oil & gas reservoir
Gas reservoir
Mud volcano
Cracks, faults & fractures
Gas from methanogenic microorganisms
$(CO_2 + H_2O \rightarrow CH_4 + CHO)$
Thermogenic oil & gas
Increasing Temperature
Jean Whelan

Bottom Simulating Reflectors (BSRs)

Bottom Simulating Reflectors (BSRs)

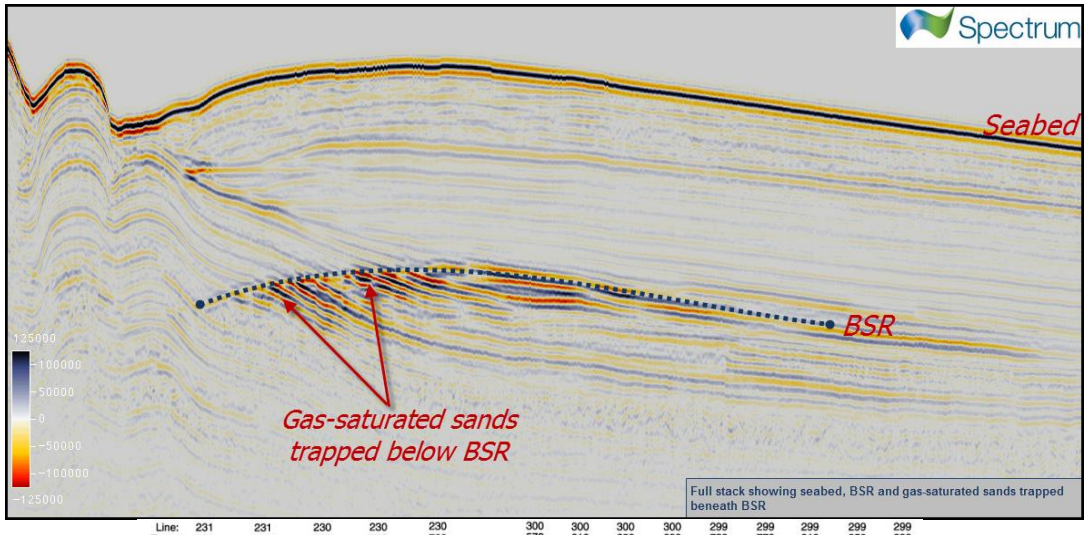

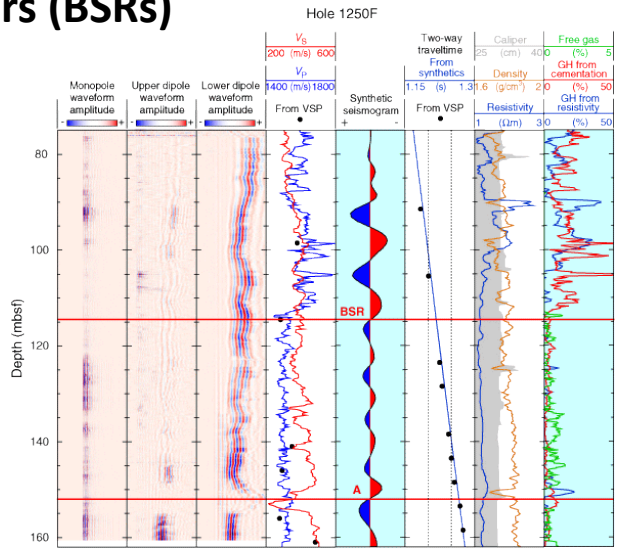

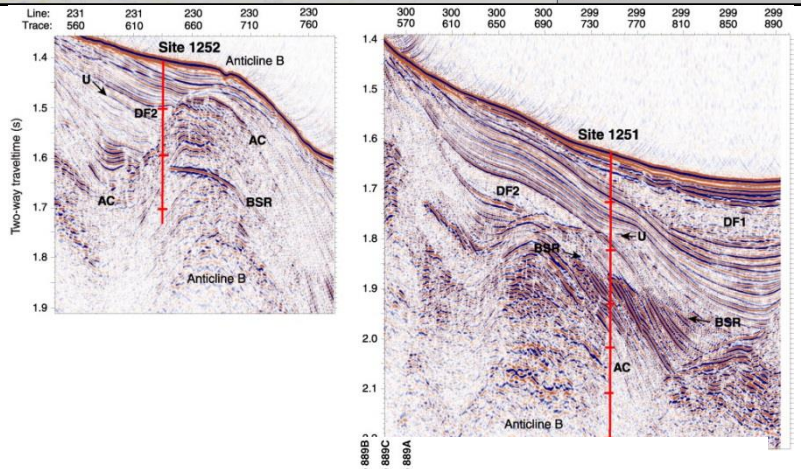

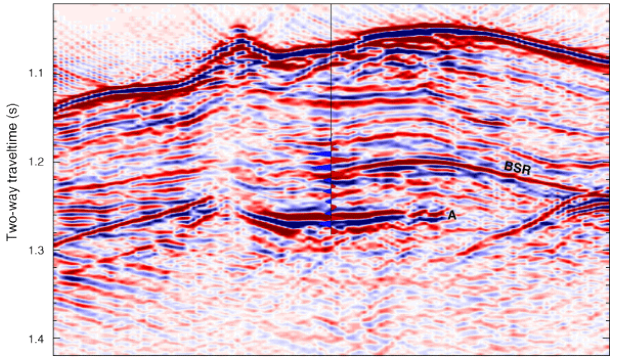

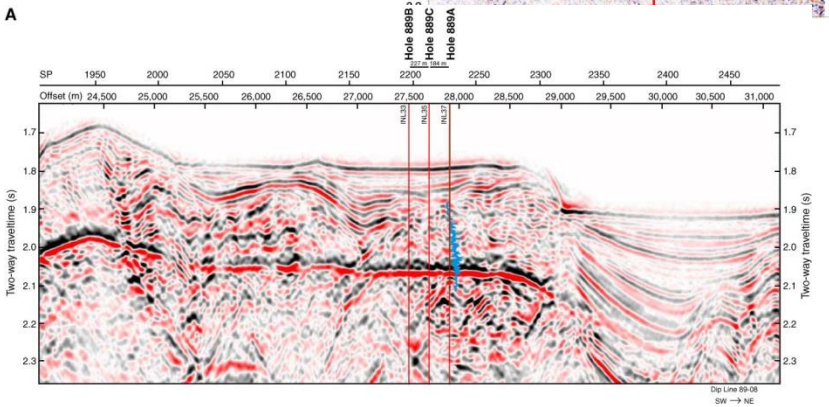

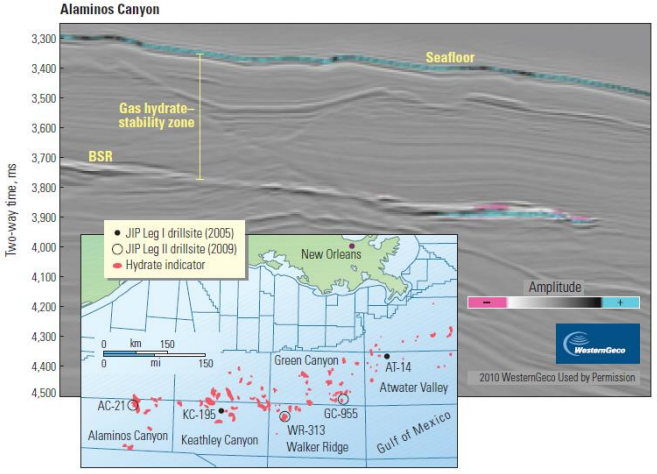

Assessment of gas hydrate stability zone and geothermal modeling of BSR in the Andaman Sea

Uma Shankar [a,*], Kalachand Sain [a], Michael Riedel [b]

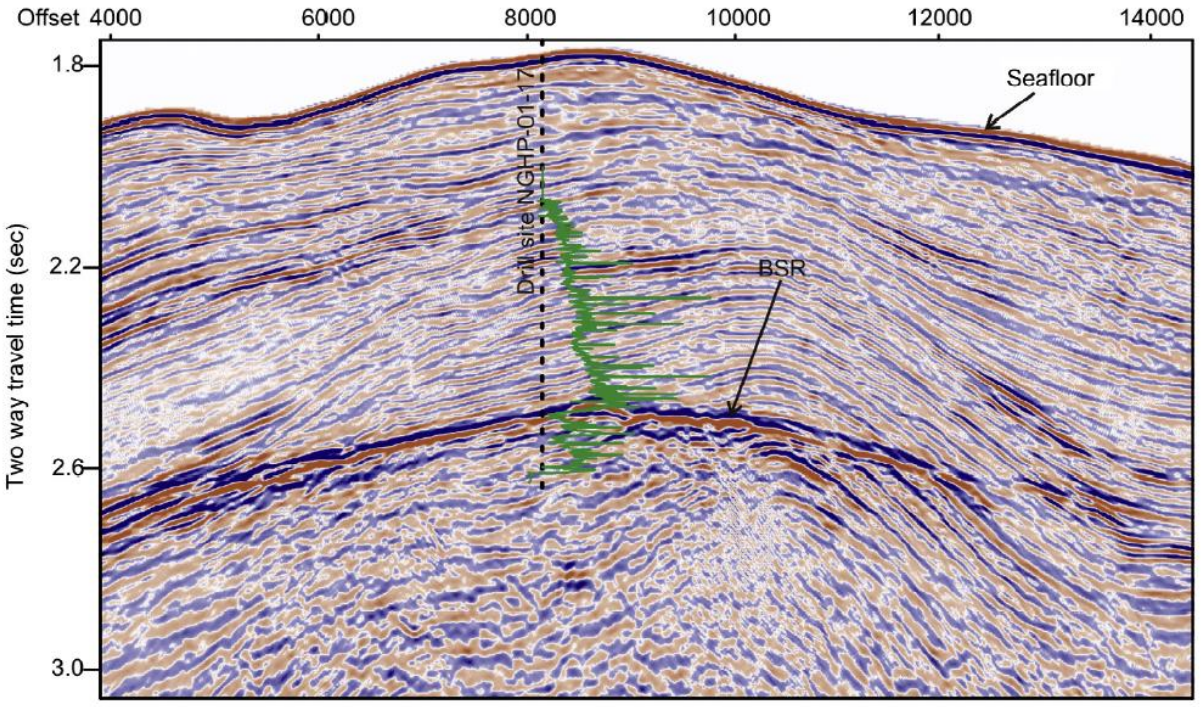

Fig. 6. 2D multi-channel reflection seismic section crossing to the drill Site NGHP-01-17 is shown. P-wave sonic velocity log superimposed on the seismic section. High velocity corresponding well with the observed BSR with high reflectivity and cross-cutting dipping reflectors.

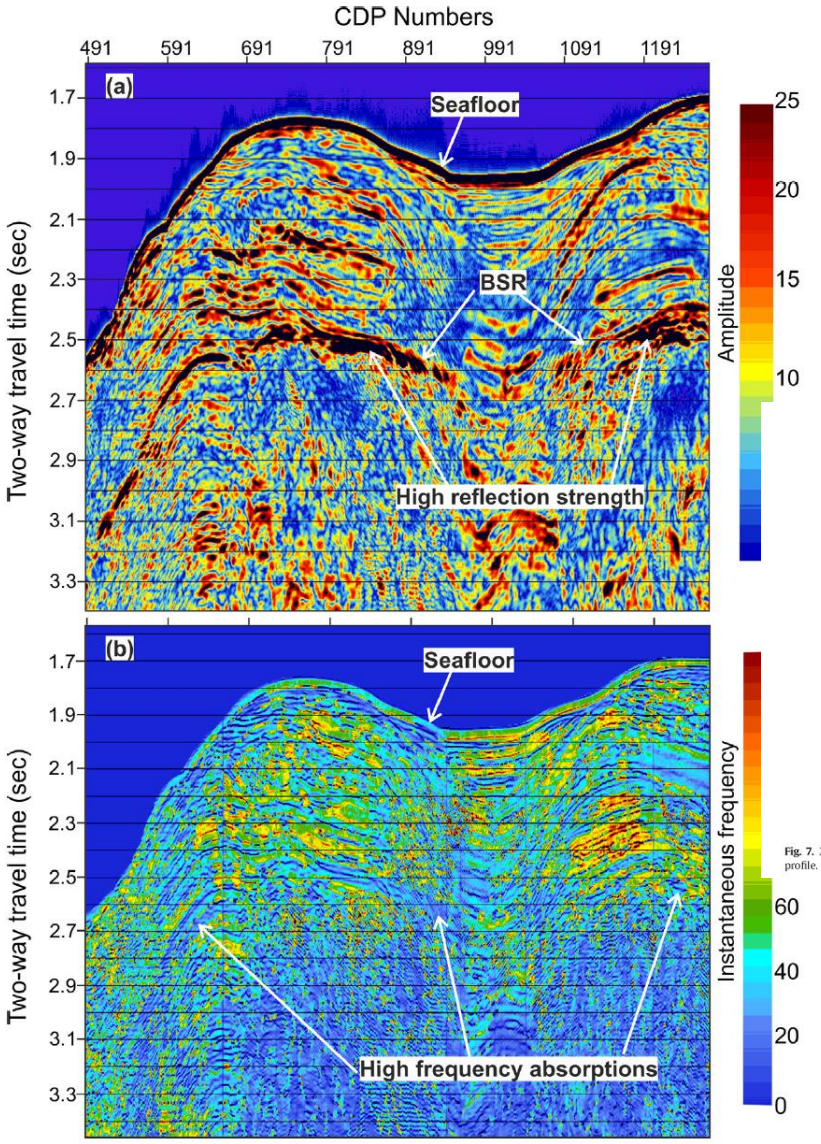

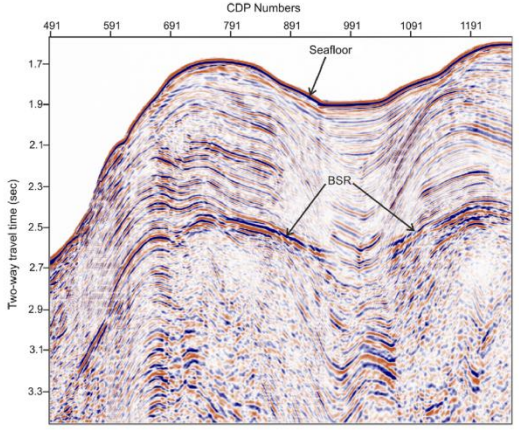

Fig. 7. 2D multi-channel reflection seismic section (oriented E–W) slightly south of the drill Site NGHP-01-17. A BSR cross-cutting sedimentary layer observed along this profile.

Fig. 8. Reflection strength amplitude of the profile shown in Fig. 7. We observe enhanced reflection amplitudes in the shallow sediments, indicating the distribution of BSRs (marked by white arrows). Additionally, the blanking zone (i.e. weak reflection amplitudes) is observed above BSRs, suggesting the occurrence of gas hydrate. (b) Instantaneous frequency of same profile shows high frequency absorption below the BSRs, indicating the occurrence of free gas.

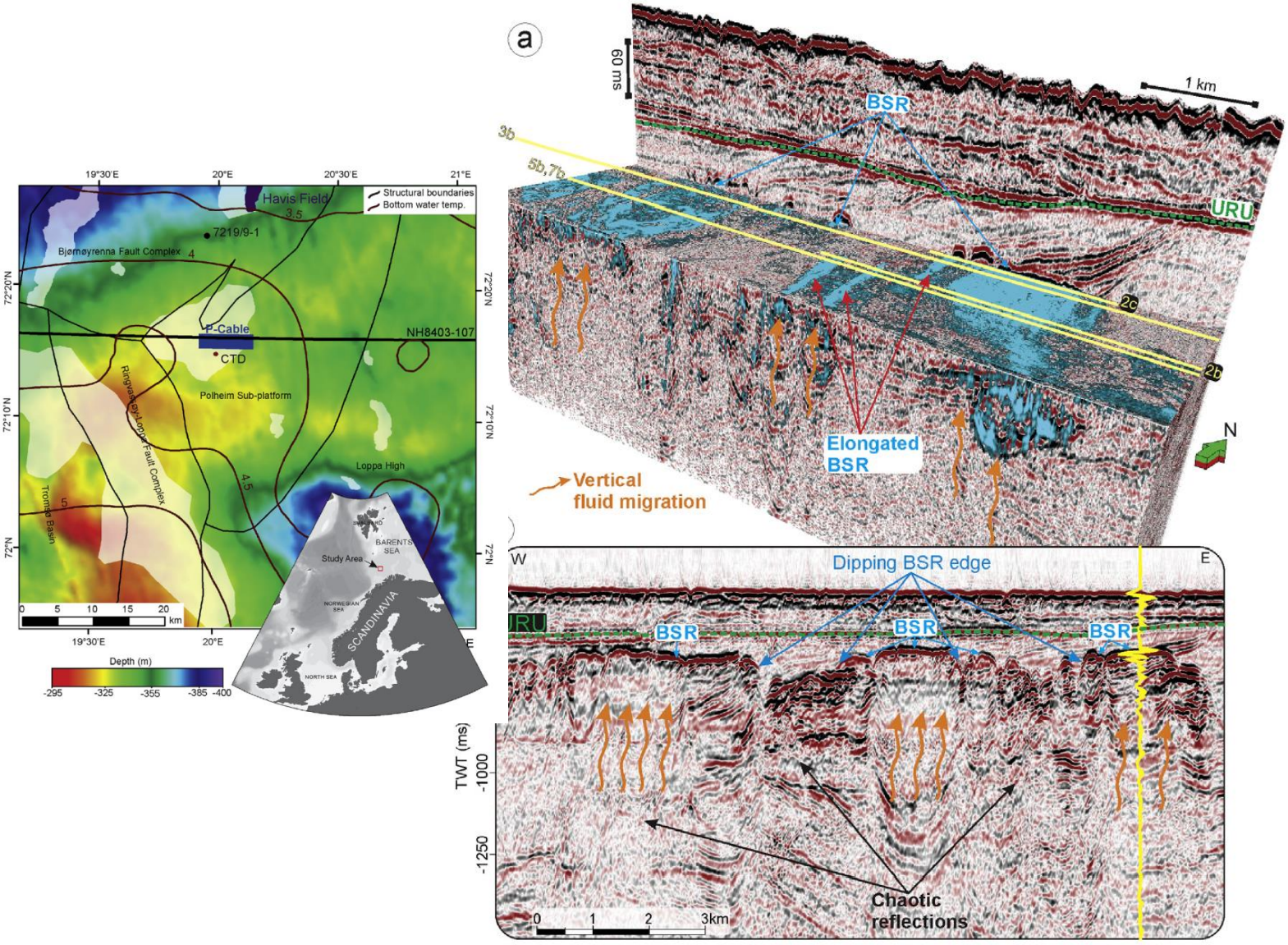

Fig. 3. a) P-Cable 3D seismic cube showing high-amplitudes (in blue) from an RMS amplitude map. It highlights the distribution of discontinuous BSRs exhibiting various shapes in the study area. b) 2D seismic profile (for location see Fig. 3a) show much wider occurrence of the BSR. It also shows the dipping edges of discontinuous BSRs. A seismic trace (yellow) shows the polarity reversal at the BSR with respect to the seafloor. (For interpretation of the references to colour in this figure legend, the reader is referred to the web version of this article.)

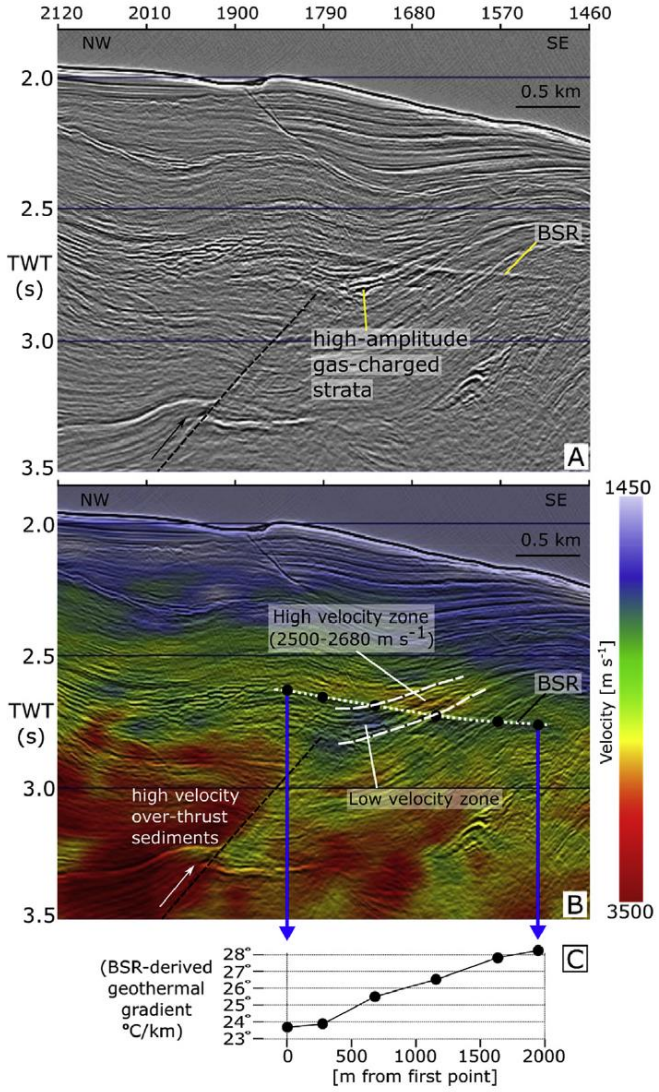

Fig. 4. A) Seismic Line 23: enlarged section of data from blue box in Fig. 3A. Thrust faults and BSR are labelled. B) Same field of view as in (A) but with seismic interval velocities (see color bar) overlaid as color shades upon the seismic reflectivity image. Annotated are: a low velocity zone caused by free gas beneath the BSR; high-velocity over-thrust sediments; a patch of high velocities directly above the BSR. Dotted white line is the BSR; broken white lines (cross-cutting the BSR) outline a sedimentary succession that hosts free gas beneath the BSR and the patch of high velocities above the BSR. Black dots are locations on the BSR used for geothermal gradient predictions shown in (C). C) BSR-derived geothermal gradients at selected locations (black dots) along the BSR. (For interpretation of the references to colour in this figure legend, the reader is referred to the web version of this article.)

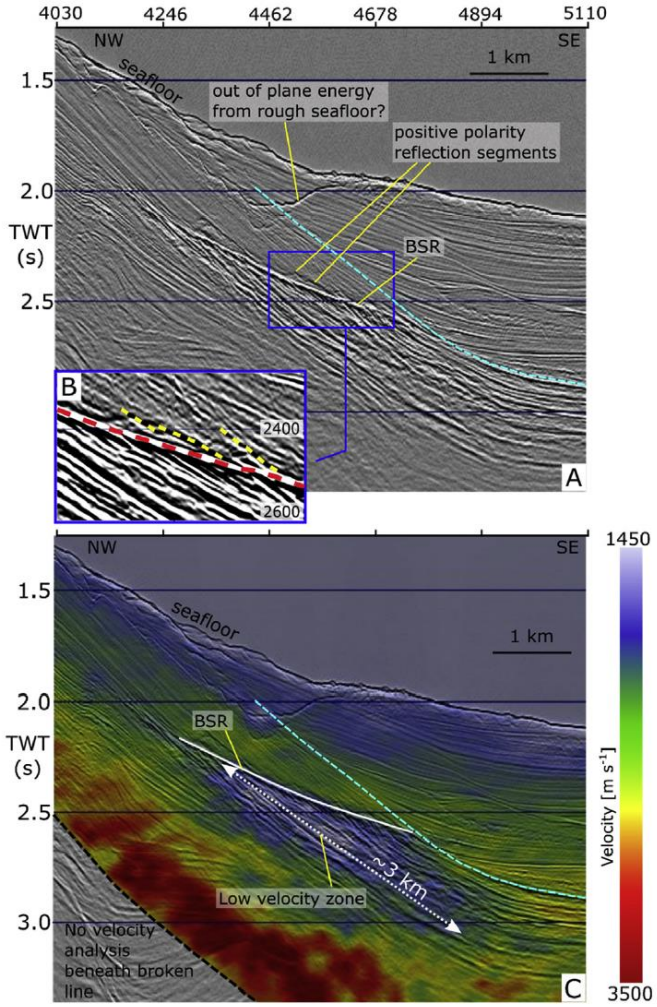

Fig. 5. A) Seismic Line 33: enlarged section of data from blue box in Fig. 3B. The BSR is labelled, as are short, positive-polarity reflections extending upward from the BSR. Broken cyan line is a sedimentary unconformity. B) Enlargement of data from blue box in (A) to highlight the BSR (broken red line) and the short, high-amplitude, positive-polarity reflections (broken yellow lines). C) Seismic interval velocities (colors) overlaid on seismic reflectivity. A thick free gas zone beneath the BSR is evidenced by the low-velocity zone. (For interpretation of the references to colour in this figure legend, the reader is referred to the web version of this article.)

dipping overlying sediments. The short, positive-polarity segments above the BSR (Fig. 5B) are too small scale to be investigated further by semblance-based seismic velocity analysis. However, the observation that these positive-polarity reflection segments lie

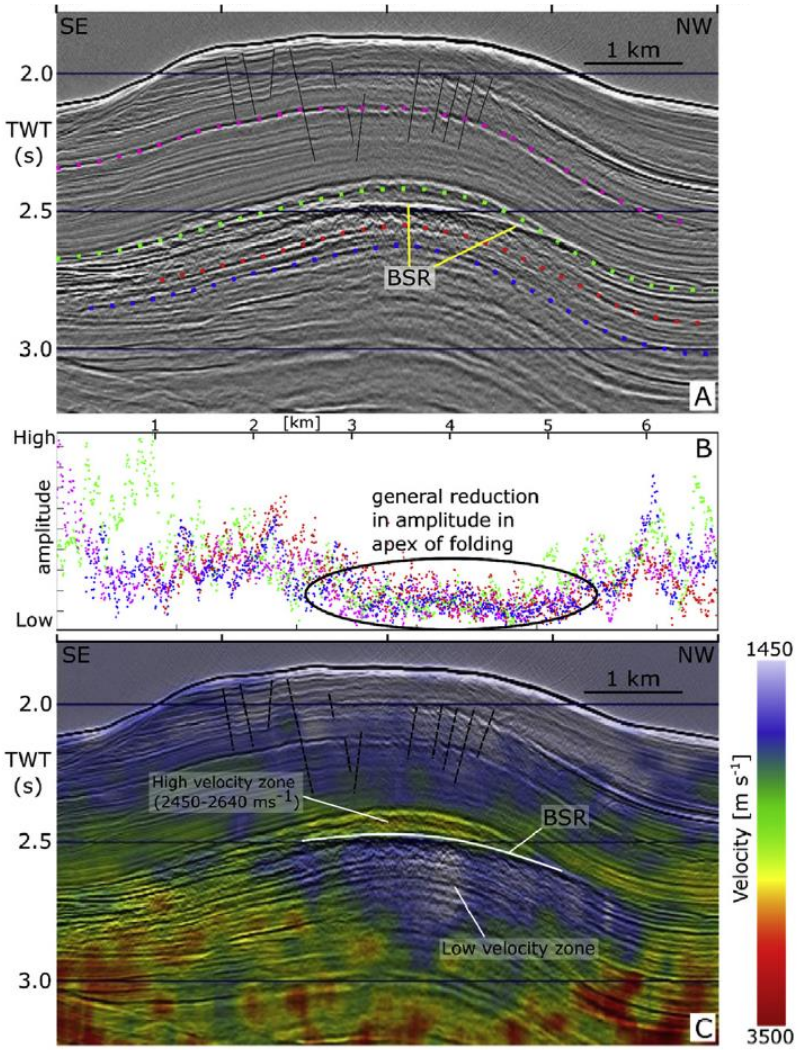

Fig. 6. A) Seismic Line 02: enlarged section of data from blue box in Fig. 3C. Normal faults beneath the seafloor are annotated by thin black lines. BSR is labelled. Colored dots trace selected reflections through the antiform structure. B) Plot of amplitude versus distance for the reflections annotated in (A). Distance scale is identical to the section in (A). Point colors match the colors used in (A). C) Seismic interval velocities (colors) overlaid on seismic reflectivity. The free gas zone beneath the BSR is evidenced by the low-velocity zone. Also annotated is a high velocity zone directly above the BSR, in the apex of the anticline. (For interpretation of the references to colour in this figure legend, the reader is referred to the web version of this article.)

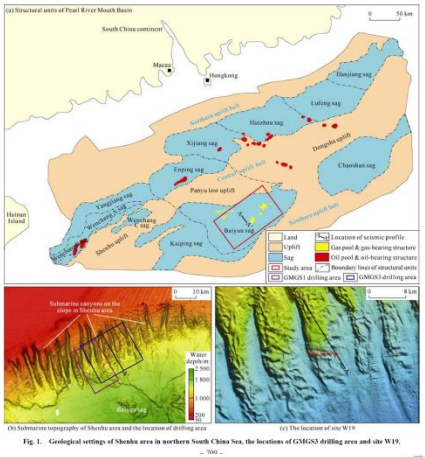

Fig. 1. Geological settings of Shenhu area in northern South China Sea, the locations of GMGS3 drilling area and site W19.

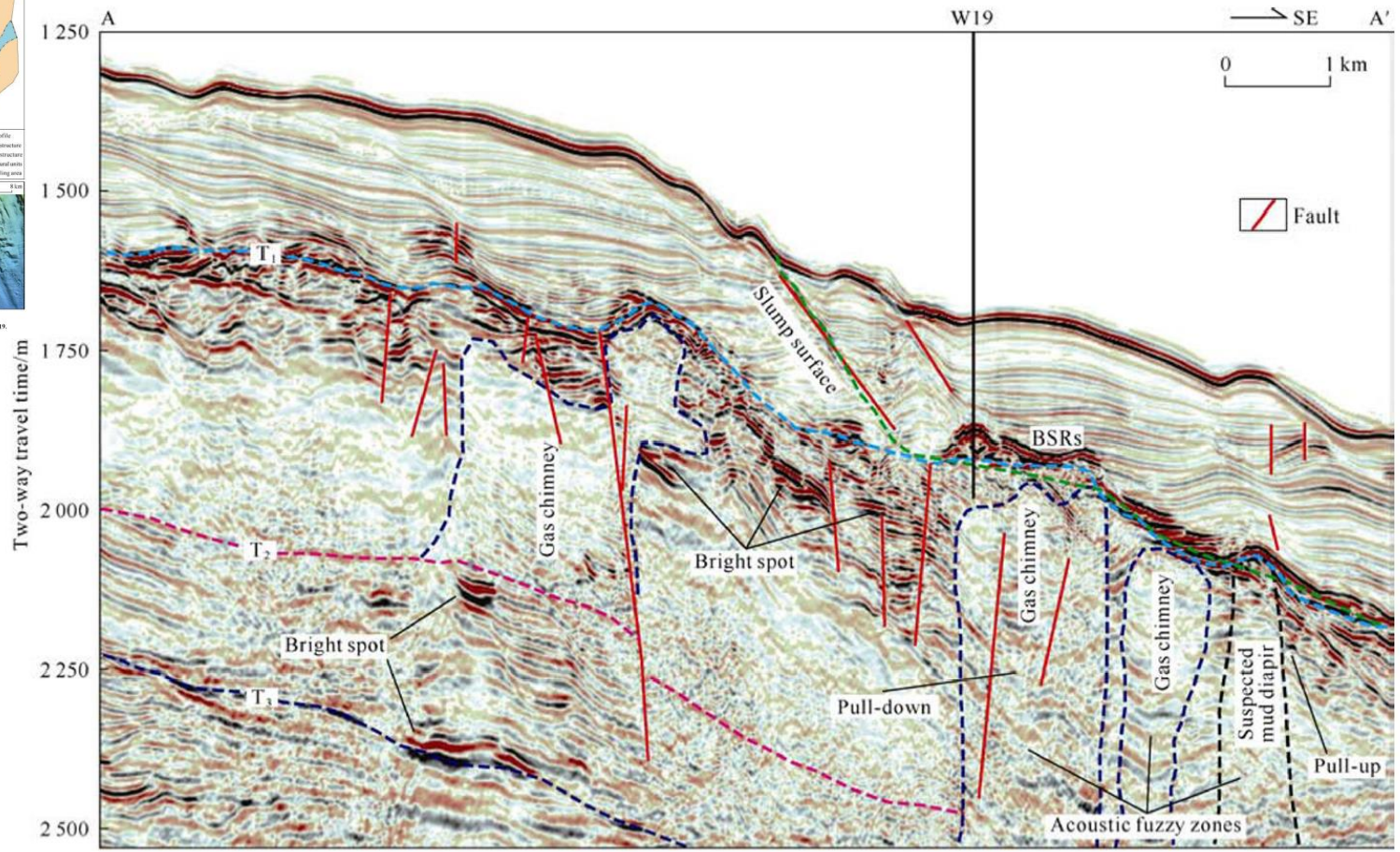

Fig. 3. Interpretation profile of site W19 in GMGS3 drilling area in Shenhu area (see Fig. 1 for the location).

A margin-wide BSR gas hydrate assessment: Canada's Atlantic margin

David C. Mosher*

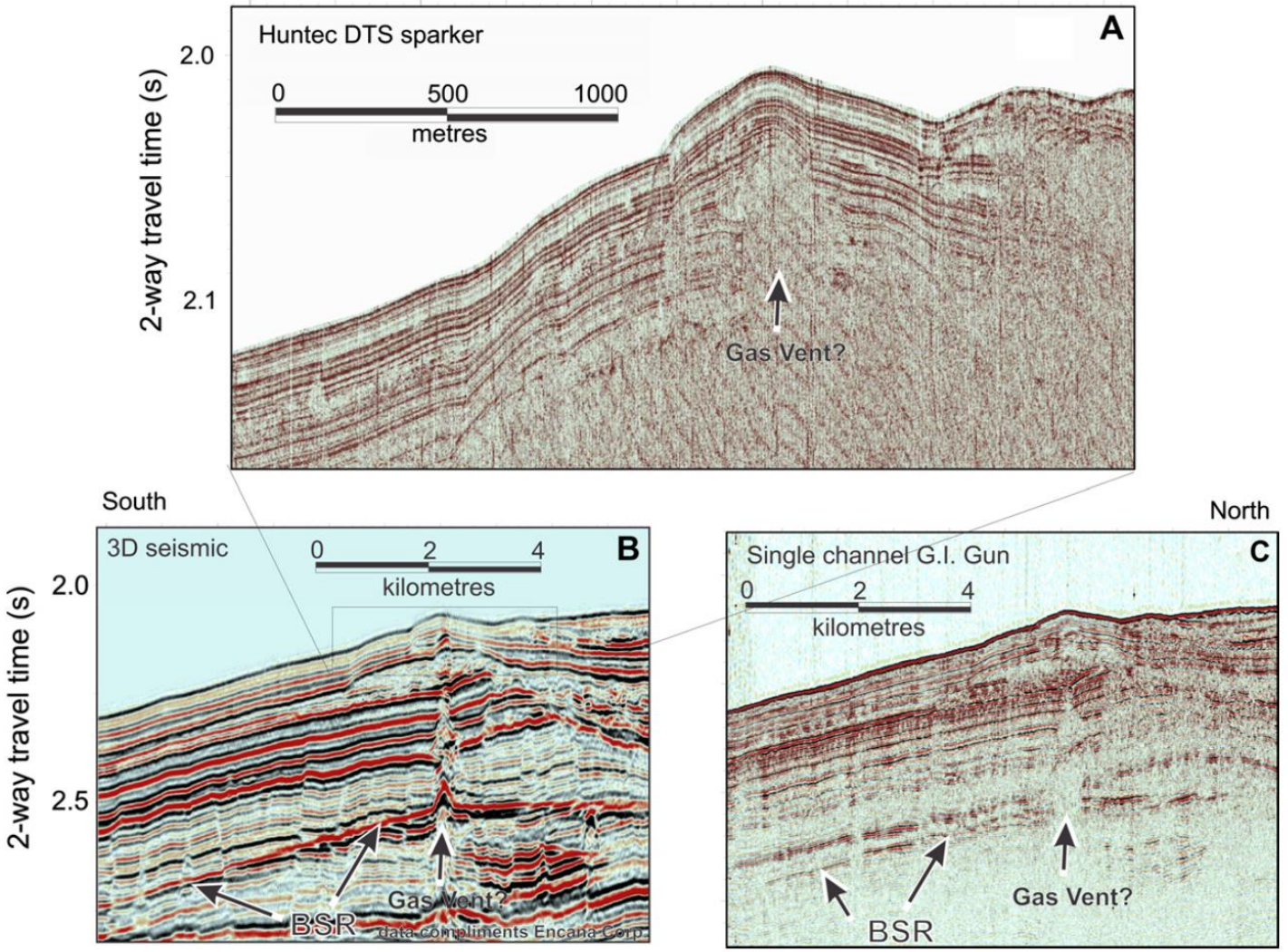

Figure 10. Possible gas or fluid vents propagate through the stratigraphic section from the gas-charged horizon shown in Fig. 8. These vents sometimes create positive relief on the seafloor. These seismic images are all from the same line across one of these seafloor mounds, but at different resolutions: A/ is an ultra high resolution (500–2500 Hz) profile (Huntec deep tow sparker), B/ is an arbitrary slice of the 3D seismic volume (5–110 Hz) (data compliments Encana Corp.), and C/ is high resolution single channel GSC seismic data (35–250 Hz). Gas masking is evident in the high resolution profiles. Note the uplifted reflector at the vent site from the 3D data (B).

Please cite this article as: Paganoni, M., Cartwright, J.A., Van Rensbergen, P., Three-dimensional seismic evidence of extensive gas hydrate deposits linked with large free gas columns suggests long-range advection mechanisms, *Marine and Petroleum Geology* (2017), doi: 10.1016/j.marpetgeo.2017.11.025.

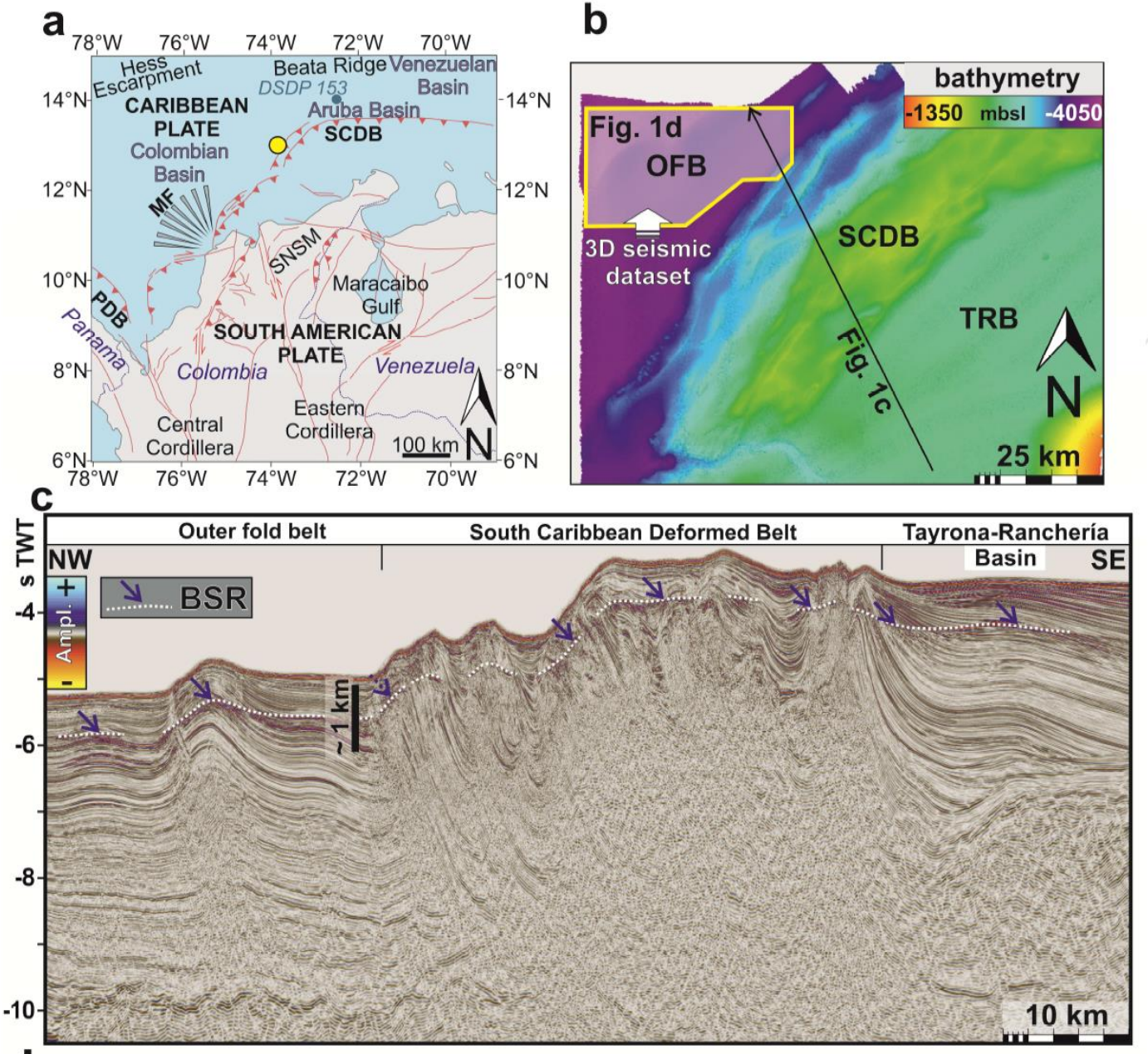

Geophysical evidence for gas hydrate accumulation related to methane seepage in the Taixinan Basin, South China Sea

Xiujuan Wang[a,b,*], Bo Liu[a,c], Jin Qian[a,b], Xin Zhang[a], Yiqun Guo[d], Pibo Su[d], Jinqiang Liang[d], Jiapeng Jin[a,c], Zhendong Luan[a], Duanxin Chen[a,b], Shichuan Xi[a,c], Chaolun Li[a]

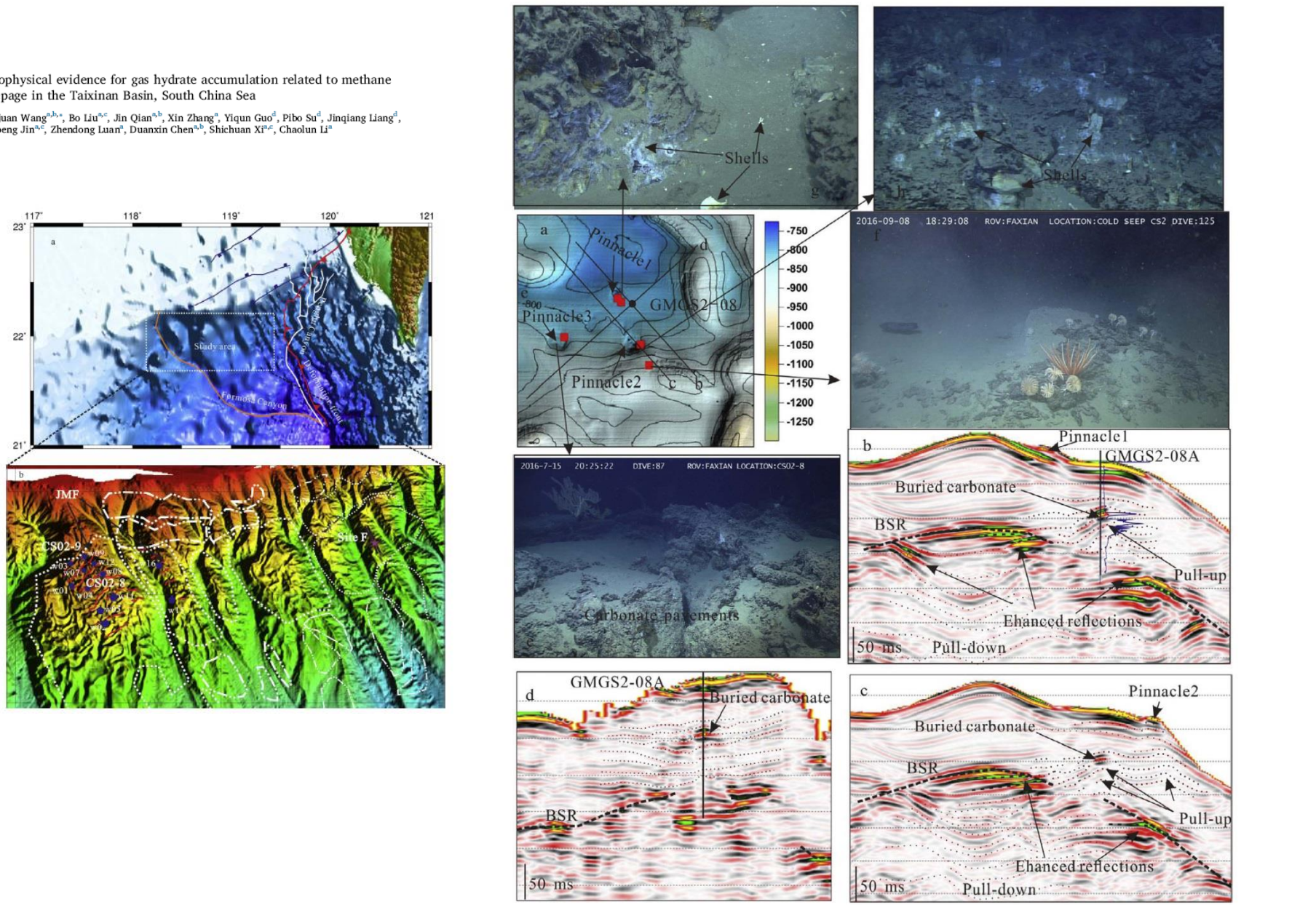

Fig. 4. (a) The high resolution bathymetry data of site CS02-8 showing pinnacles near Site GMGS2-08, and locations of seismic sections in b–d; (b) Seismic section through Site GMGS2-08 and Pinnacle 1 showing the BSR, the high amplitude reflections of buried carbonate layer; Enhanced reflections and pull-down reflection indicating the presence of free gas below the BSR. The P-wave velocity log was plotted by the synthetic seismogram. (c) Seismic section through pinnacle 2 and buried carbonate layer; (d) Crossline seismic section through Site GMGS2-08; (e) Seafloor images for Pinnacle 3 showing carbonate pavement; (f) seafloor image showing coral and sea anemone; (g) Seafloor images for Pinnacle 1 showing the dead shells, mud bottom and carbonate blocks; (h) carbonate mixed dead shells and mud sediment.

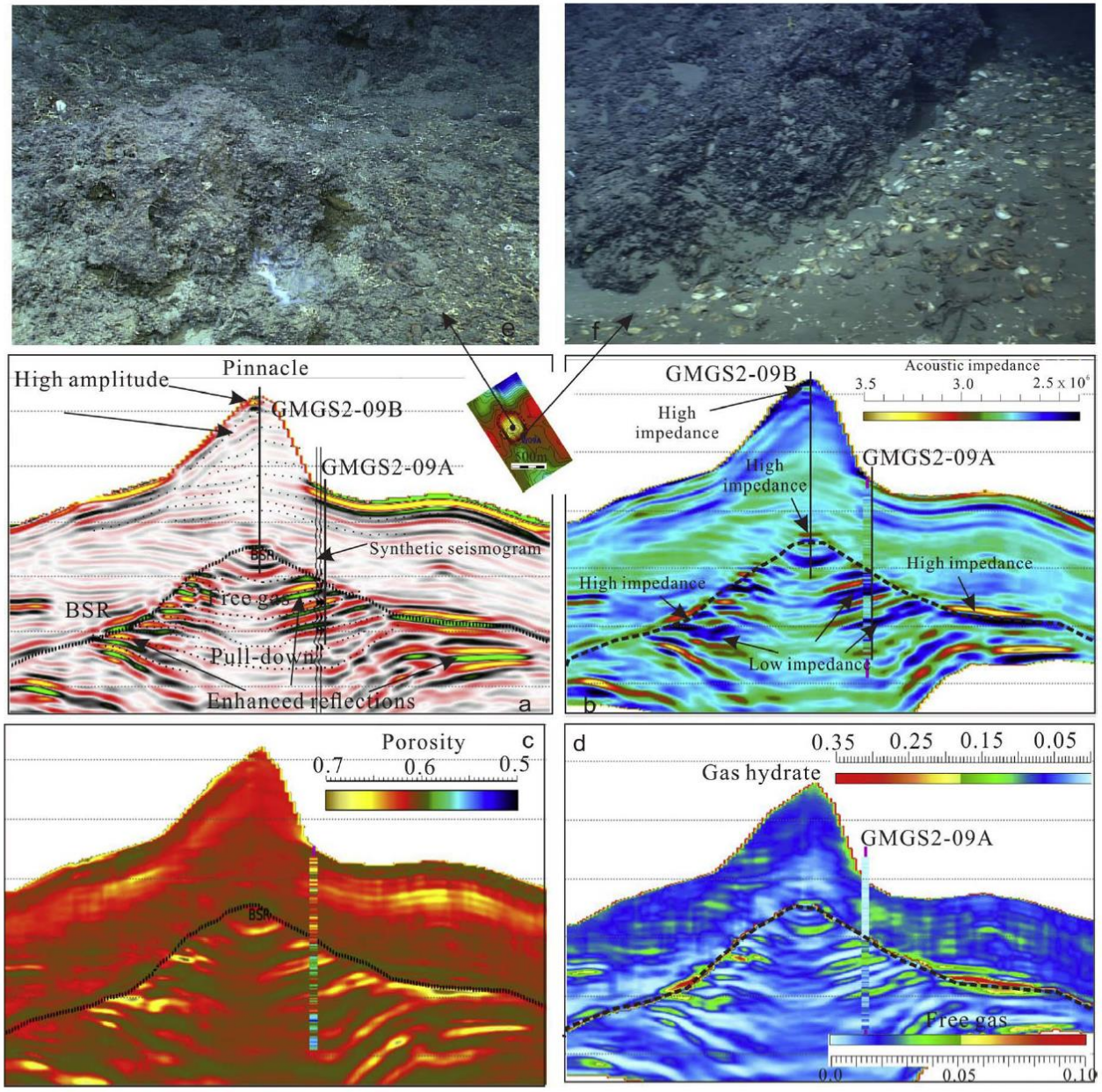

Fig. 5. (a) Seismic section through Site GMGS2-09 showing carbonate mound, the discontinuous BSR, and enhanced reflections, pull-down reflection below the BSR at Site CS02-9. Insert is the seafloor map showing the size of the pinnacle; (b) The inverted acoustic impedance and the well log P-impedance with color display; (c) Porosity profile used to calculate free gas and gas hydrate saturations; (d) Gas hydrate saturation and free gas saturation with patchy model estimated from the acoustic impedance and porosity; (e) Seafloor images showing the carbonate rocks and dead biology; (f) Seafloor carbonate mixed with mud sediments and abundance of dead shells.

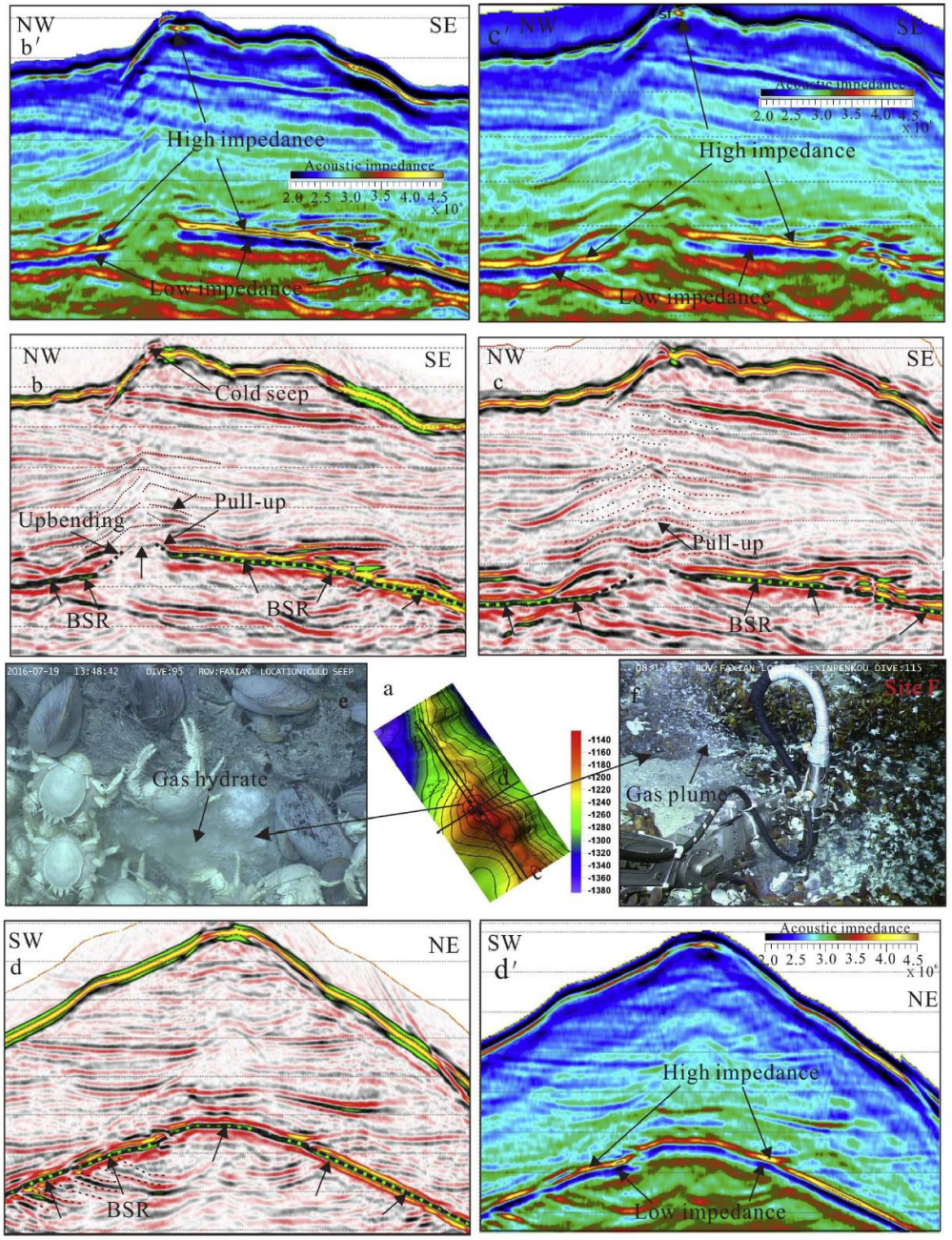

Fig. 8. (a) The high resolution bathymetry data at Site F and locations of seismic sections in b–d; (b–d) Seismic sections through Site F showing the continuous BSR and pull-up reflections and acoustic blanking above the BSR; (b'–d') The inverted acoustic impedance sections showing high acoustic impedance above the BSR and low acoustic impedance below the BSR; (e) The exposed gas hydrate; (f) Densely packed mussels and crabs at Site F and ongoing methane bubbles.

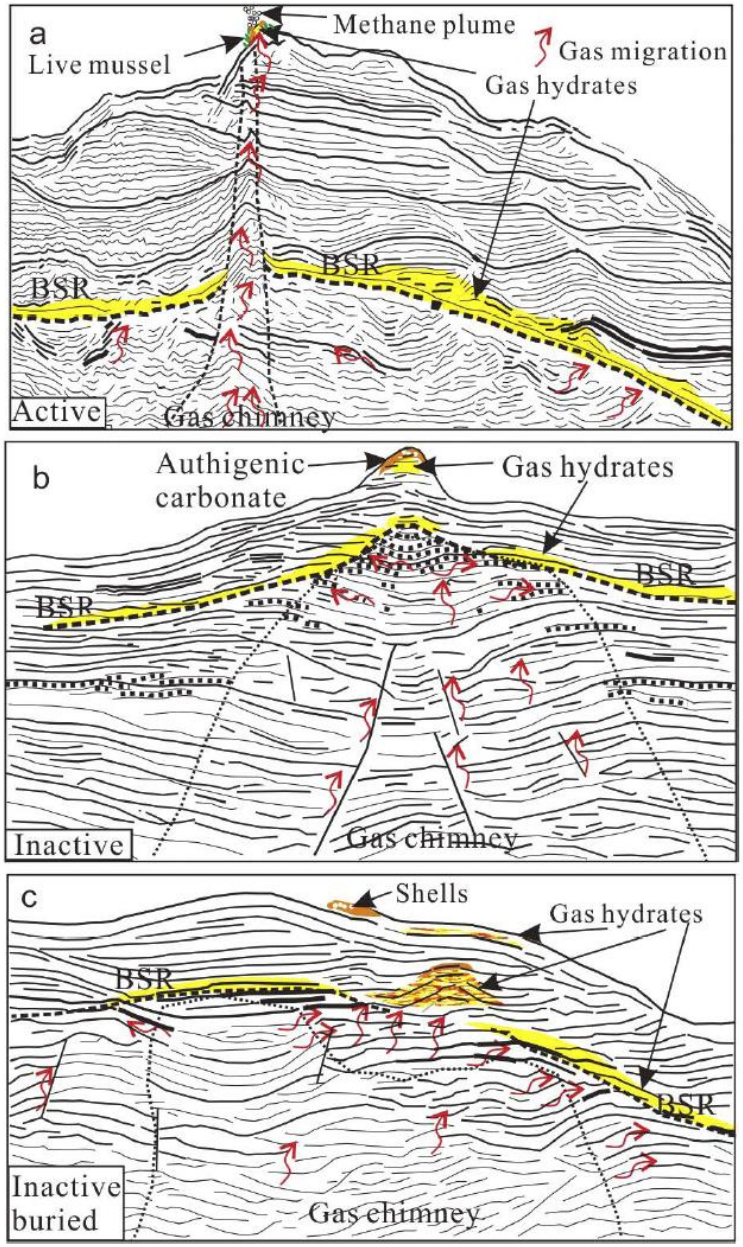

Fig. 9. Schematic representations showing the different development stages of cold seeps system. (a) The active cold seep; (b) The inactive cold seep system; (c) The buried cold seep system and the new formed cold seep.

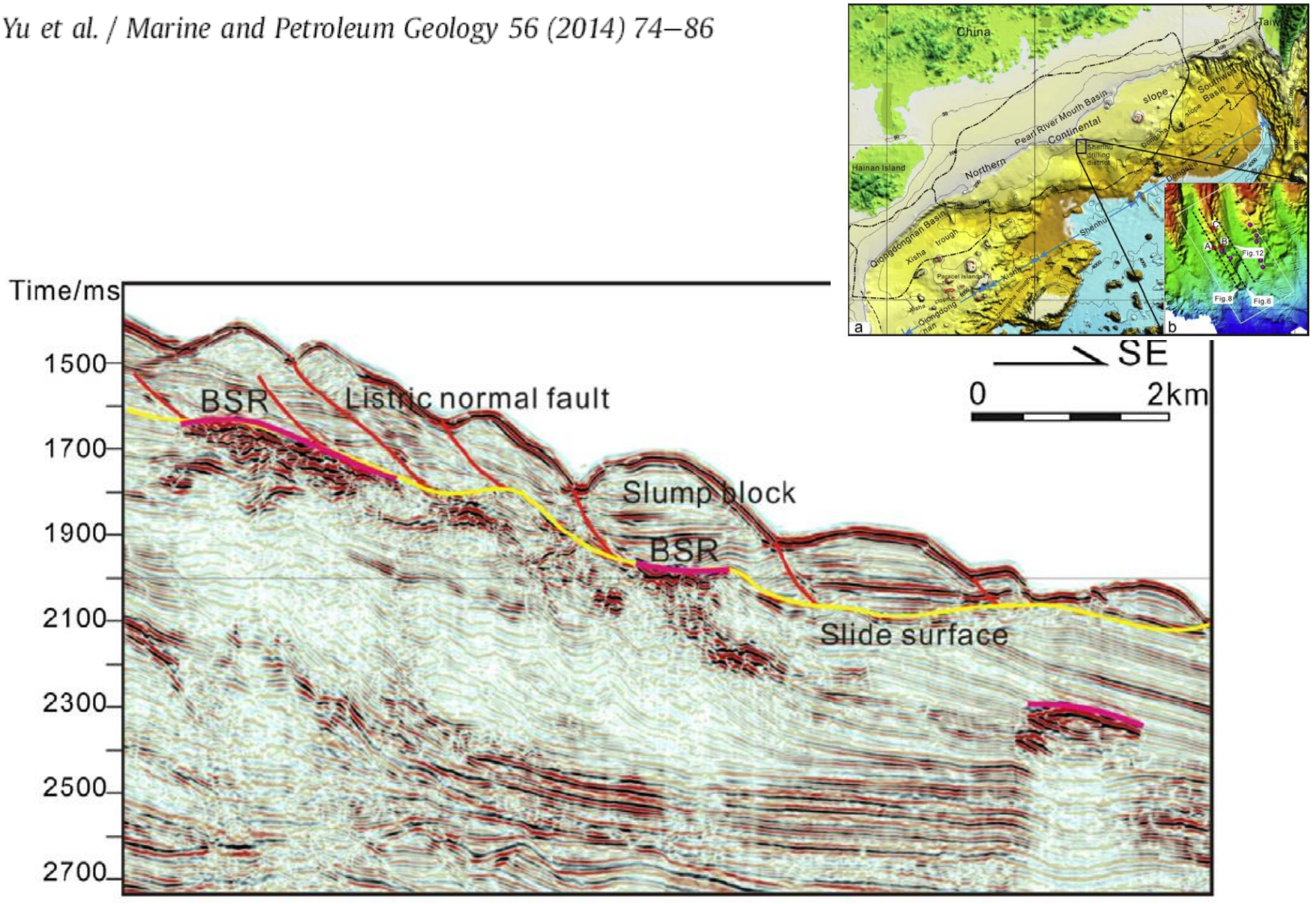

Figure 12. The listric normal fault and associated slump block in Shenhu drilling district of SCS. The location of the seismic profile is shown in Figure 1.

Application of AVO attribute inversion technology to gas hydrate identification in the Shenhu Area, South China Sea

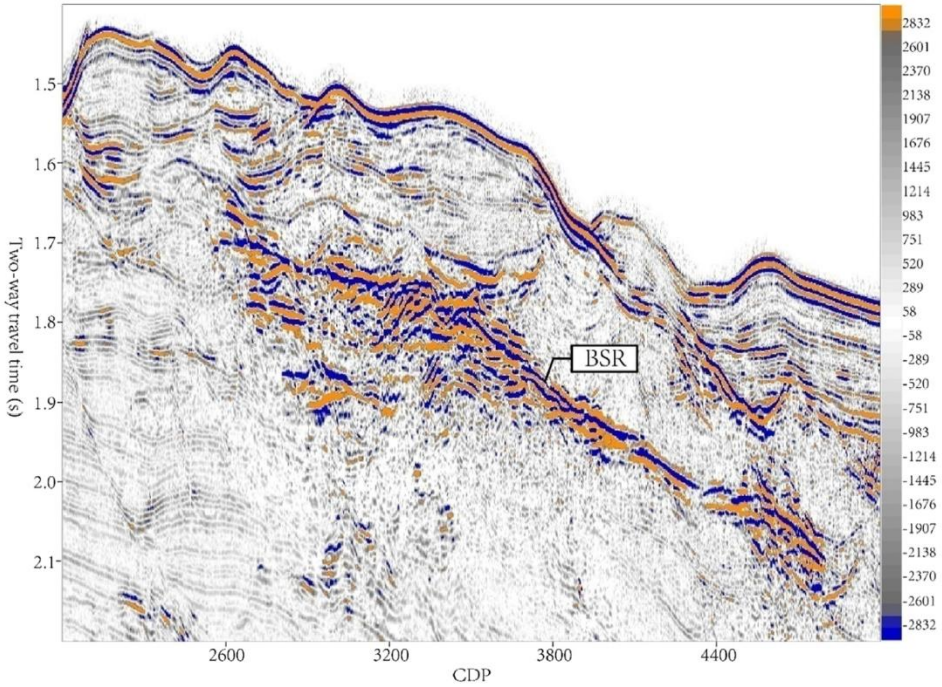

Fig. 8. The fluid factor profile.

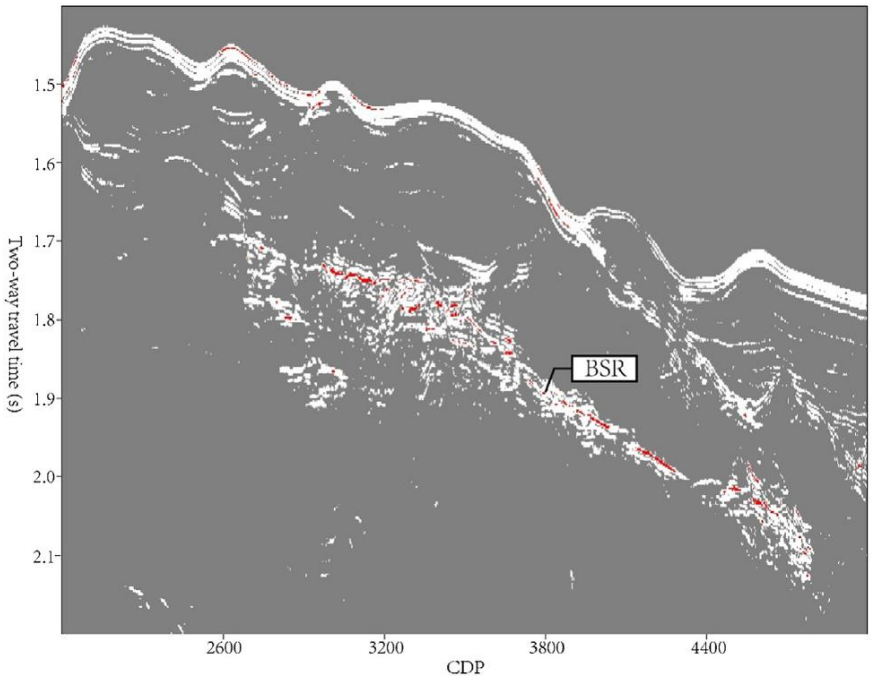

Fig. 11. AVO anomaly recognized by cross plot analysis is stacked on the seismic profile.

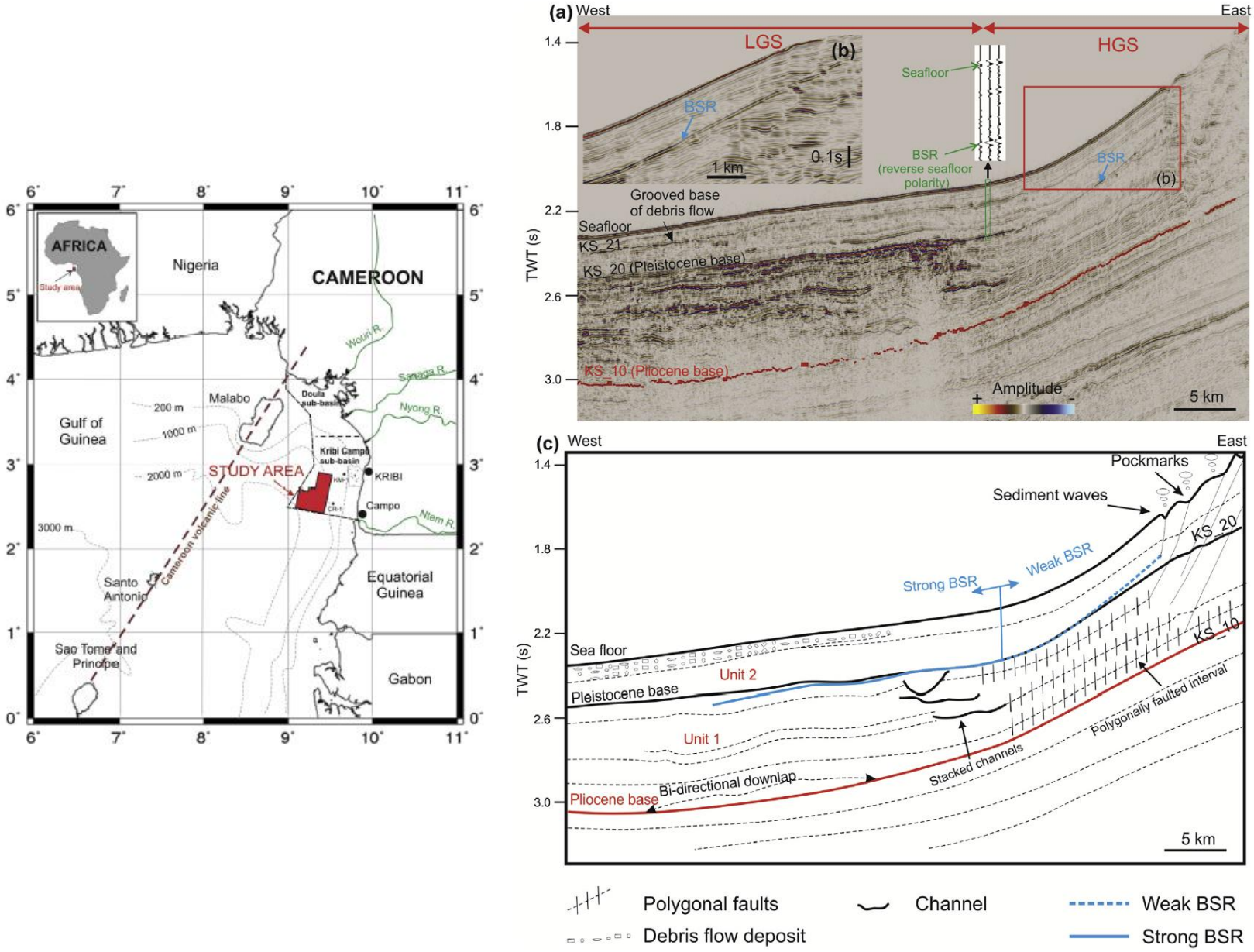

Figure 4. Seismic profile downslope along gully 4 and interpreted line drawing illustrating overview of the stratigraphy and main structural elements of the study area, defined by two slopes, High Gradient Slope (HGS) and Low Gradient Slope (LGS) (see Fig. 2 for the location map). In unit 1 (from KS_10 to KS_20), the LGS is characterized by the alternation of low to high amplitude reflections associated with the vertical stacked channels; the HGS shows low amplitude reflections associated with the polygonal faults and E-flowing gullies which associated with sediment waves. The upper unit (from KS_20 to the seafloor) is dominated by low amplitude reflections in both slopes. While the LGS is highly modified by the debris flows and sliding, the HGS experienced less deformation but does contain a gully system.

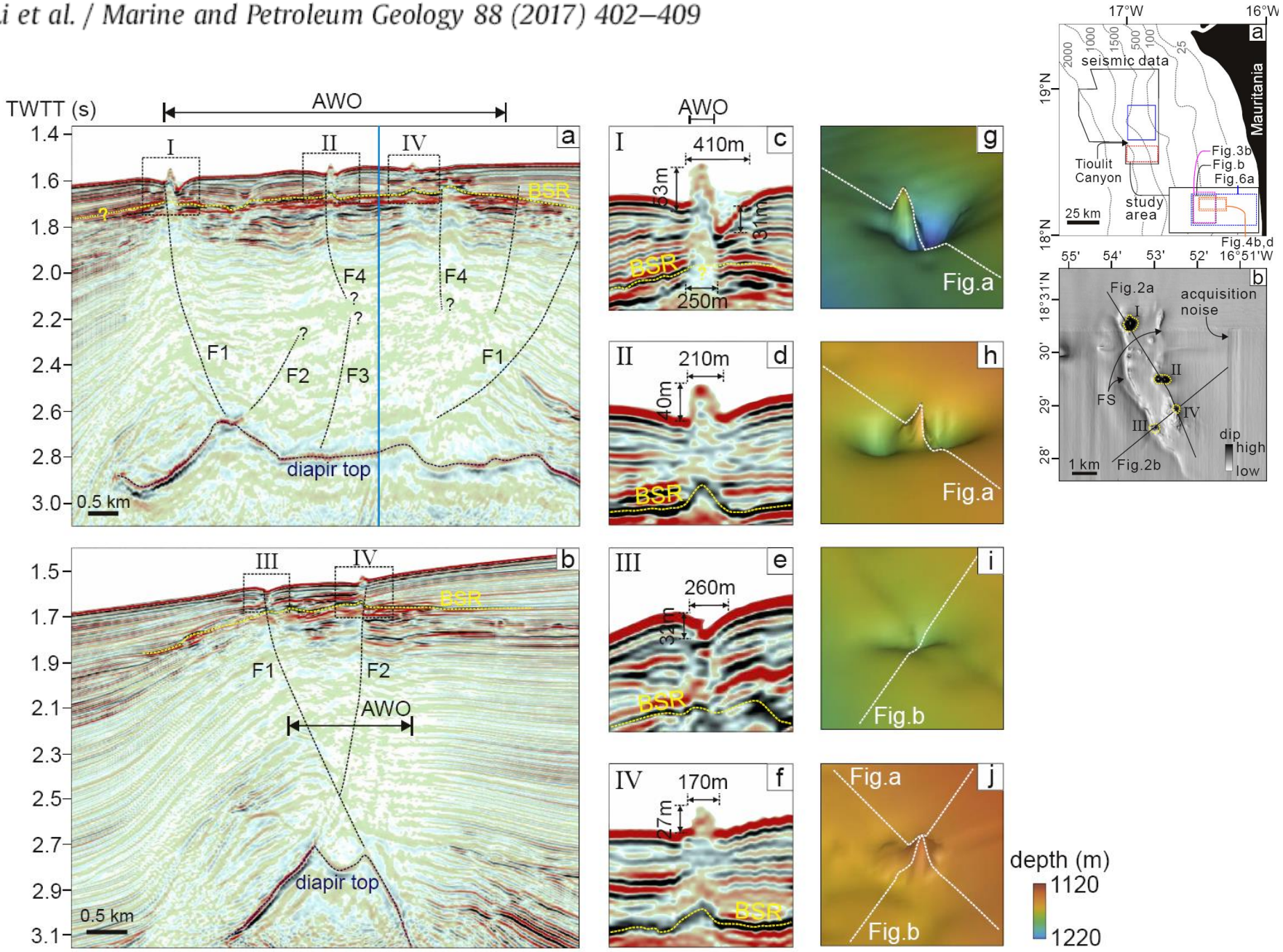

Fig. 2. (a–b) Representative seismic cross sections displaying the spatial relationship between the reliefs at the seabed, the faults and the salt diapir. The acoustic wipe-out (AWO) shows up below I-IV and in the zone bounded by F1, F2 and F4. (c–f) Zoom-in figures showing the cross-sectional geometry of I-IV. (g–j) 3-D imaging of the bathymetry exhibiting the morphology of I-IV.

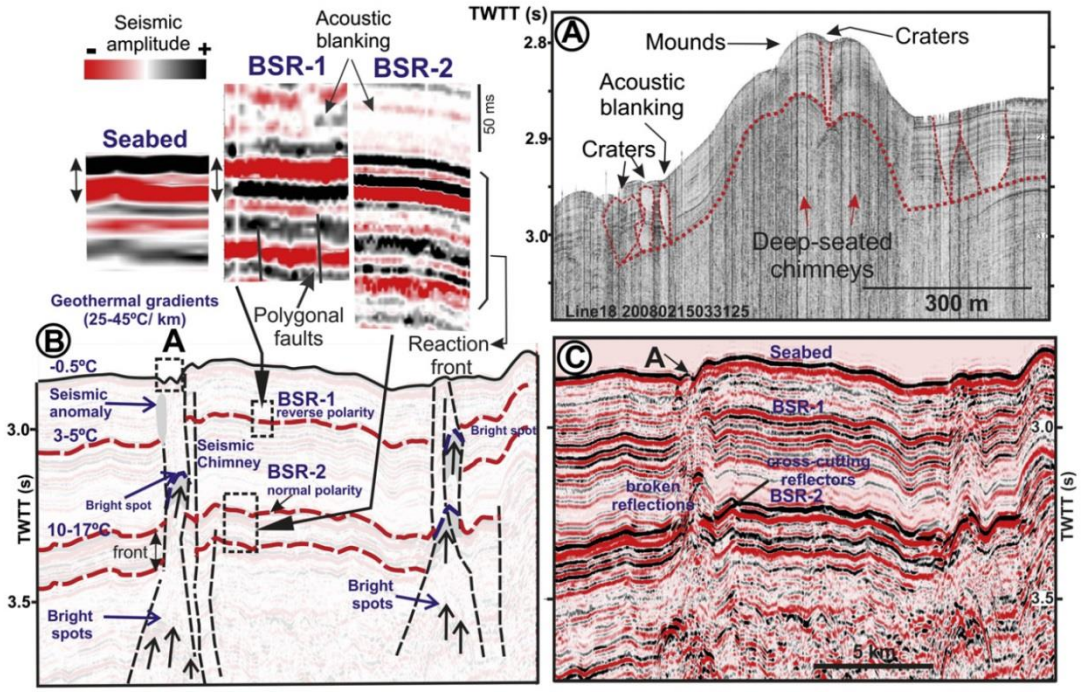

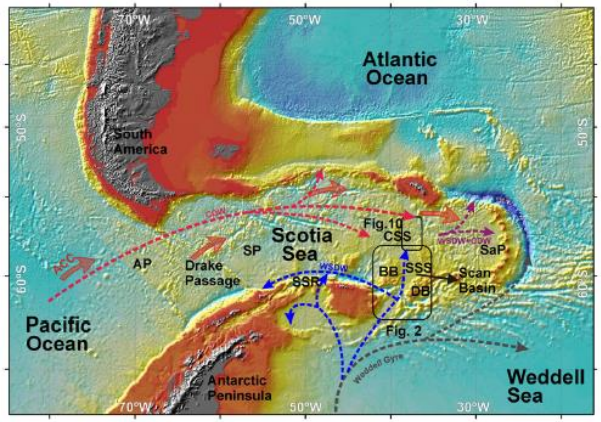

Fig. 5. (A) HRS profile of a seabed mound and a crater located in the central Scotia Sea; and (B) corresponding MCS profile IT89AW39 and line drawing (C). Calculated temperatures and detailed amplitude polarity for BSR events are also shown. Seismic chimneys that breach distinct BSRs underlie seabed mounds and crater features. See location in Figs. 2 and 4.

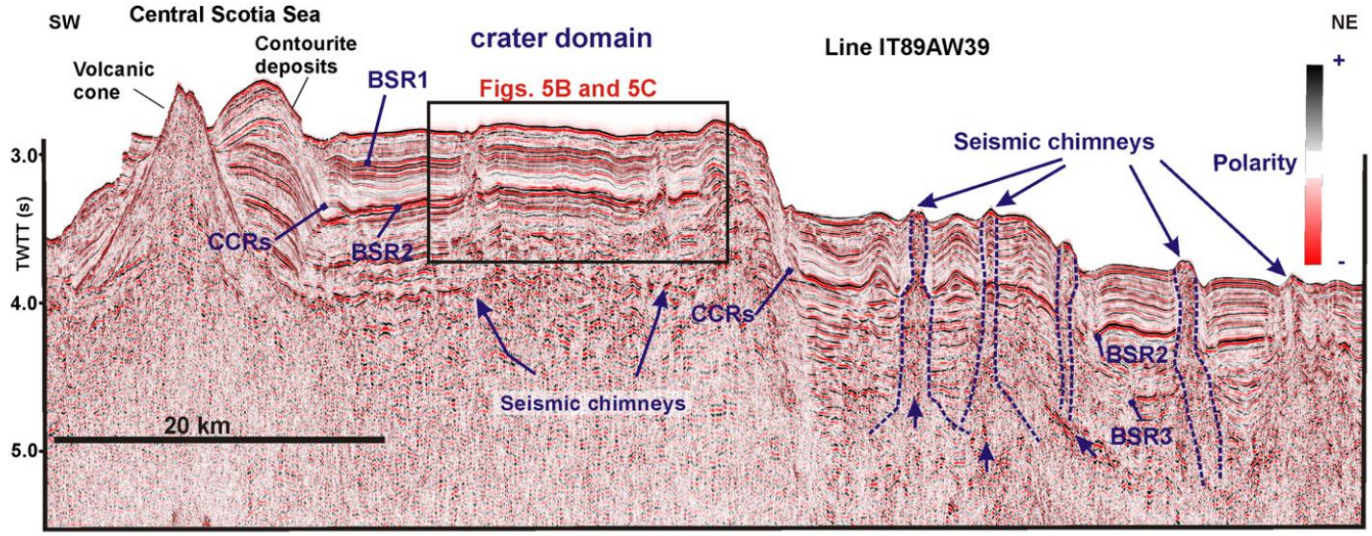

Fig. 4. MCS profile IT89AW39 in the northwestern Discovery Bank (central Scotia Sea) (a). Black box indicates the location of a detailed section and corresponding line drawing shown in Fig. 4. See location in Figs. 2 and 3D.

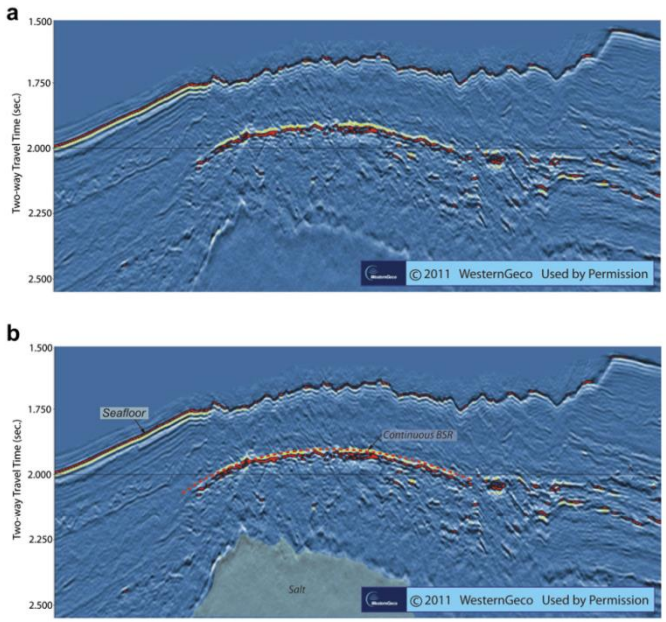

Figure 4. Example of continuous BSR from Garden Banks 982. (a) Un-interpreted profile. (b) Interpreted profile with red dashed line indicating inferred BSR and BGHS. Data© 2011 WesternGeco. Used by permission. (For interpretation of the references to colour in this figure legend, the reader is referred to the web version of this article).

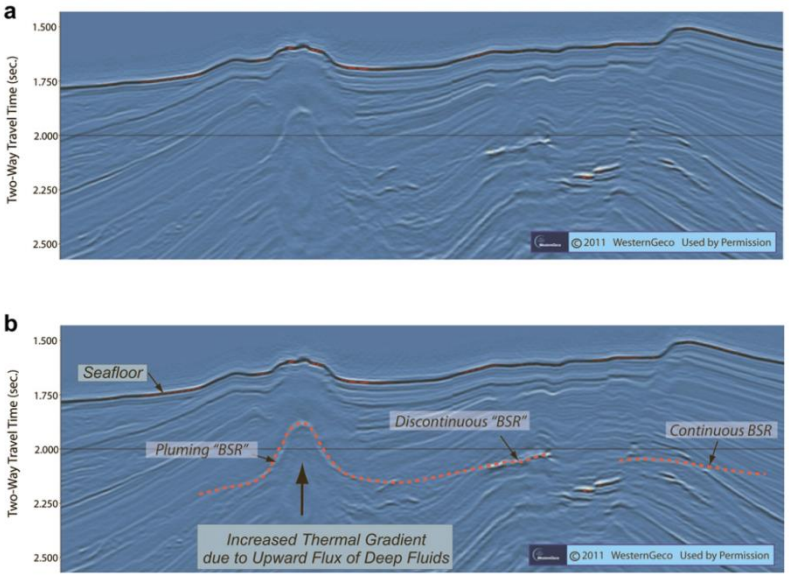

Figure 5. Example of pluming BSR (left side of image) from Green Canyon 475. Continuous BSRs are present to the center and right. (a) Un-interpreted profile. (b) Interpreted profile with red dashed line indicating inferred BSR and BGHS. Data© 2011 WesternGeco. Used by permission.

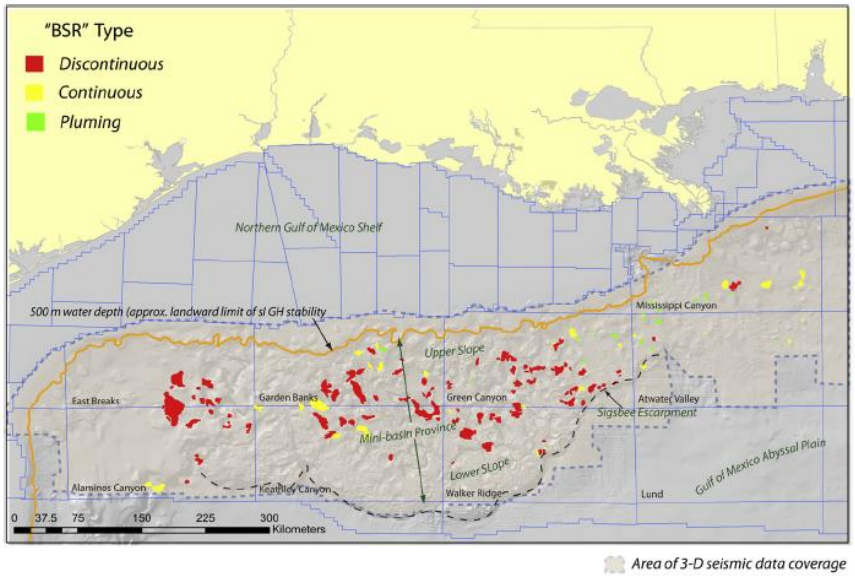

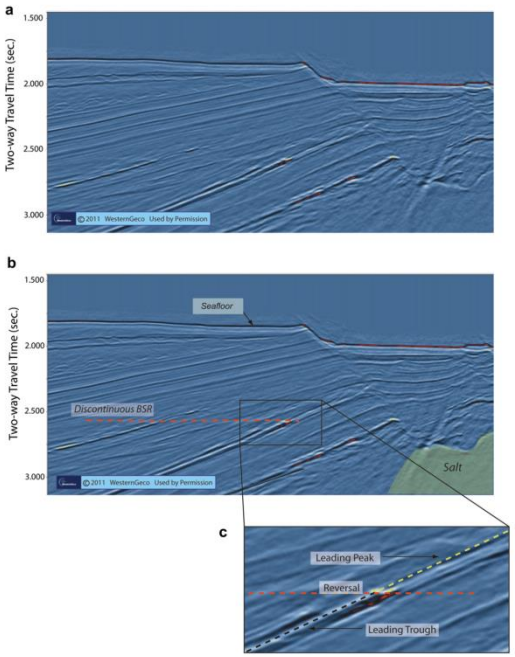

Figure 11. Seismic data from Green Canyon 781 showing a discontinuous BSR with phase reversals at two horizons. (a) Un-interpreted profile. (b) Partially interpreted profile. Data© 2011 WesternGeco. Used by permission.

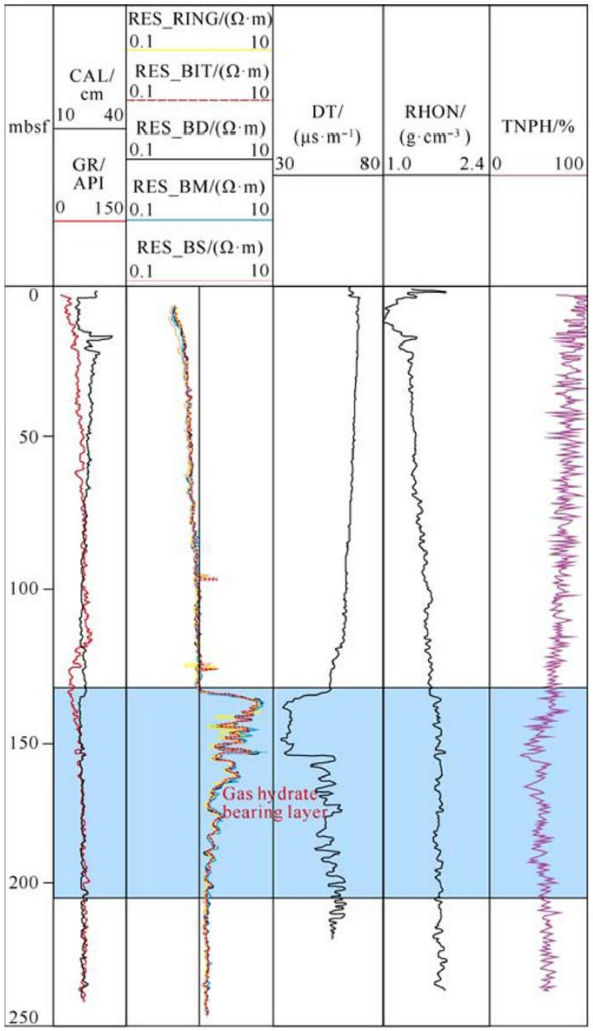

Fig. 5. Logging response of pilot borehole of site W19 in GMGS3 drilling area.

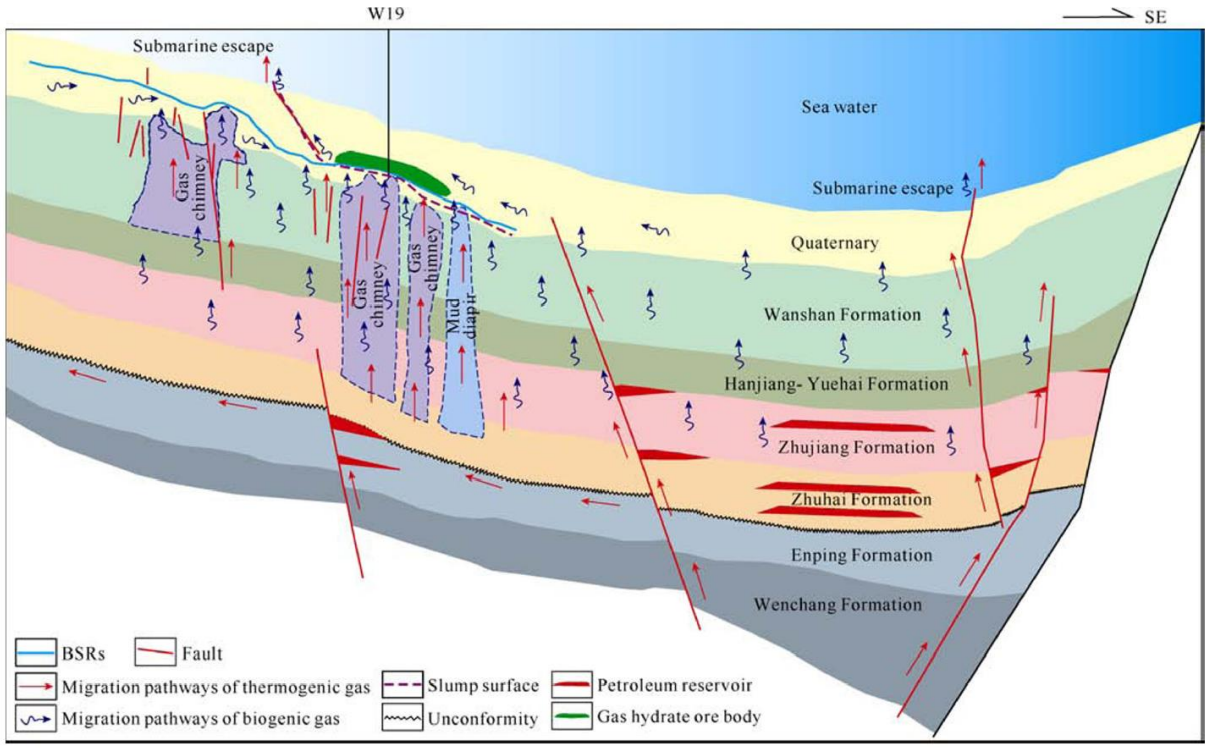

Fig. 9. Migration and accumulation model of gas hydrate with high saturation of site W19 in GMGS3 drilling area in Shenhu area.

Gas hydrate formation in compressional, extensional and un-faulted structural settings – Examples from New Zealand's Hikurangi margin

H. Wang [a], G.J. Crutchley [b, *], T. Stern [a]

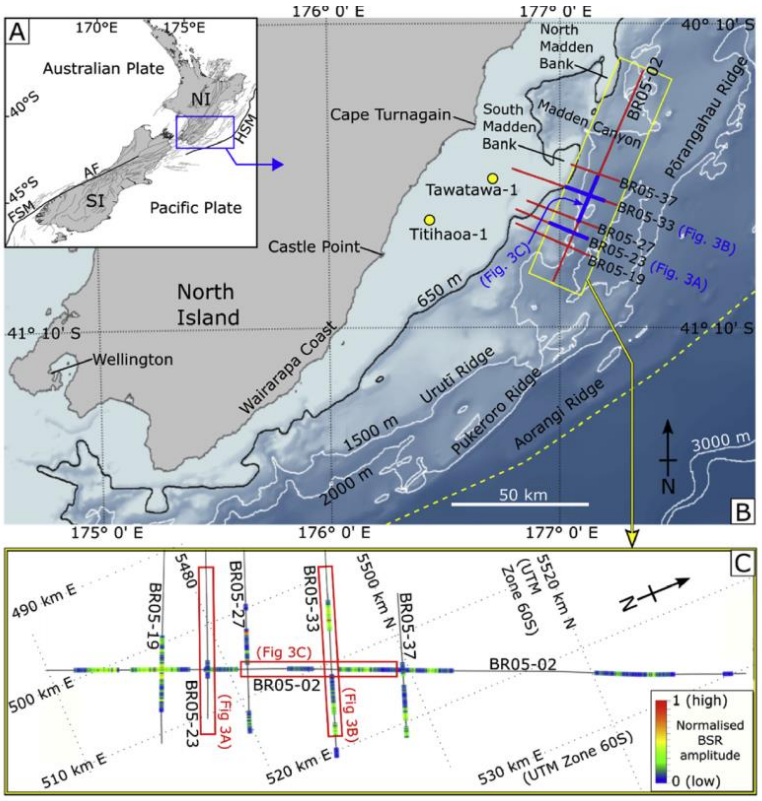

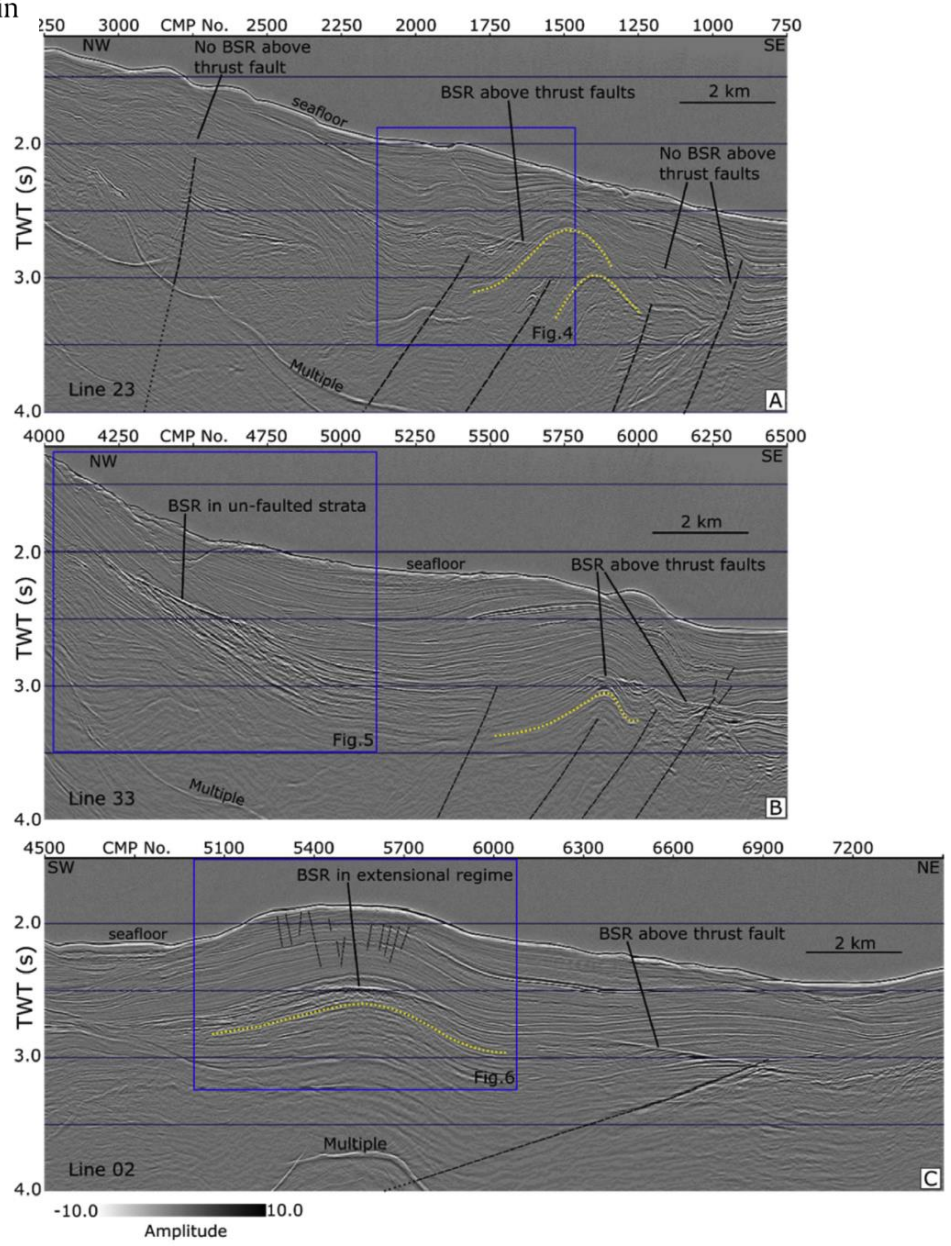

Fig. 3. A) Selected section of Seismic Line 23. Thrust faults are annotated by broken black lines. Antiform folding is highlighted by dotted yellow lines. A bottom-simulating reflection (BSR) is labelled. **B)** Selected section of Seismic Line 33. Annotations as in (A). **C)** Selected section of Seismic Line 02. Annotations as in (A) and (B), except that shallow faults within the antiformal folding are normal faults. (For interpretation of the references to colour in this figure legend, the reader is referred to the web version of this article.)

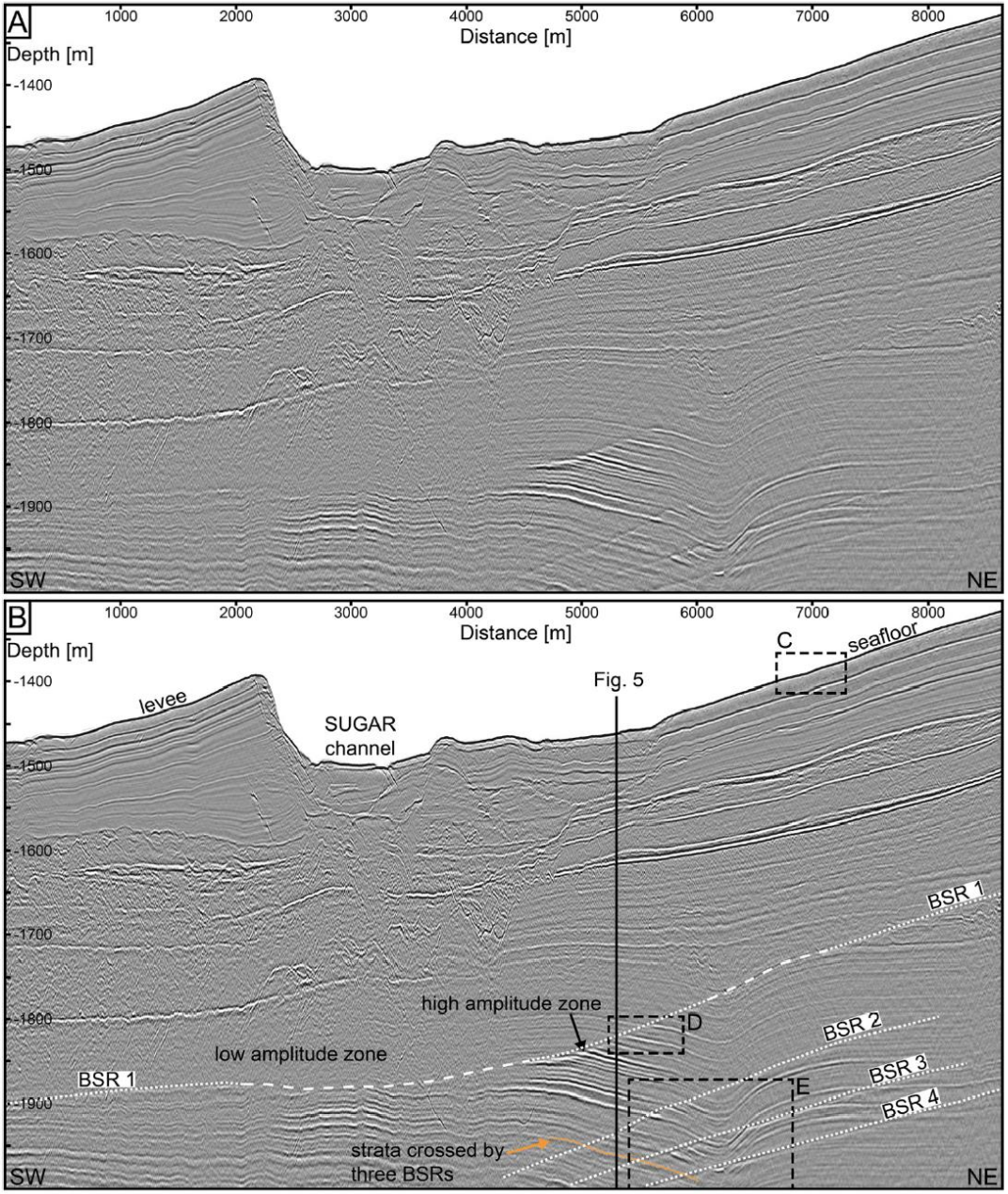

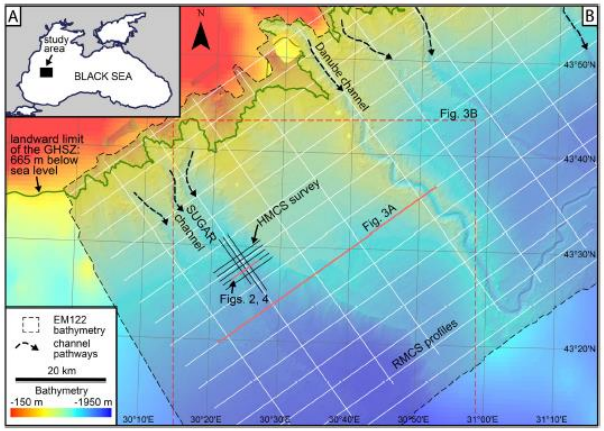

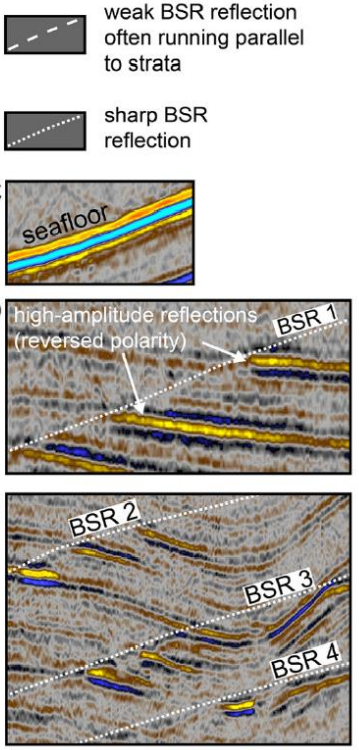

Fig. 2. A: 2D HMCS line 1107 across the SUGAR channel-levee system. The location is shown in Fig. 1. B: Interpreted section showing the general character of the four stacked multiple BSRs. C–E: Insets with different color scale highlight the positive polarity of the seafloor (C) and the negative polarities of the reflections underneath the shallowest BSR 1 (D) and BSRs 2–4 (E).

Минералы опал и кристобалит и их фазовые переходы

Опа́л (от санскр. उपलः (upalaḥ) — «камень» через др.-греч. ὀπάλλιος и лат. *opalus*) — минералоид, аморфный кремнезём $SiO_2 \cdot nH_2O$ (гидрат диоксида кремния), широко используемый в ювелирном деле

Кристобалит — минерал, высокотемпературная полиморфная модификация кварца или низкотемпературная тетрагональная псевдокубичная модификация кремнезема координационного строения — SiO_2

Опал - преимущественно или только аморфный кремнезем - SiO_2nH_2O, с переменным содержанием воды, с низкой плотностью (около2,1), растворимый в КОН, с низким показателем преломления (чаще всего от 1,38 до 1,46). Опал биоскелетов имеет n = 1,440 ±0,002, что соответствует содержанию воды около 9%. Опал обнаружен только в кайнозойских и мезозойских силицитах, а в более древних - он замещен кристаллическими формами кремнезема, в основном, халцедоном и кварцем.

Кристобалит SiO_2 низкотемпературный полукристаллический тетрагональной или псевдокубической сингонии с низким преломлением и двупреломлением (почти изотропный), существующий при температуре до 200-275ºС, обычно коллоидальный по размерам кристалликов, пластичный или волокнистый, метастабильный, растворяется в расплавленной Na_2CO_3. В седиментогенных и метасоматических опалитах более распространен неупорядоченный кристобалит, который понимается неодинаково и называется по разному. По-видимому, это непрерывный стадийный ряд раскристаллизации рентгеноаморфного биоморфного и хемогенного опала (опал А) - от почти чистого опала с зачаточными кристаллами до чистого кристобалита или тридимит-кристобалита.

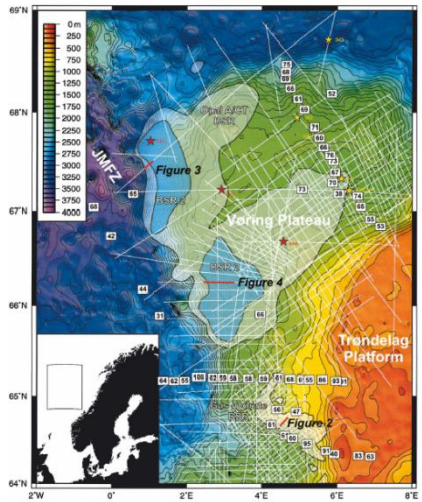

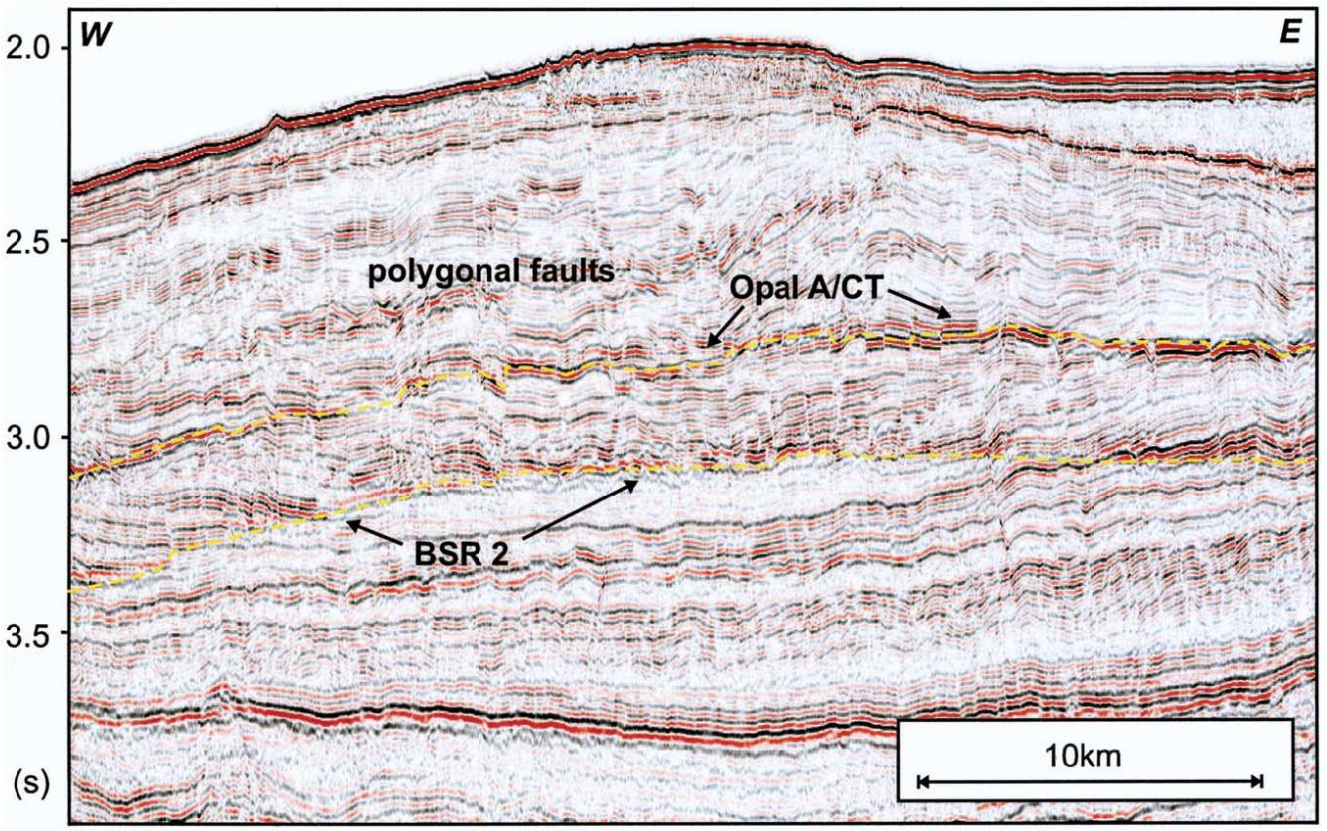

Fig. 4. Seismic example of the diagenesis BSR. Note the offset of the opal A/CT BSR where it is intersected by the polygonal faults indicating that it was deformed after its diagenetic origin.

Abstract

Three classes of bottom simulating reflectors (BSR) cross-cut the post-breakup sediments of the mid-Norwegian margin. The first class is caused by free gas at the base of the pressure- and temperature-dependent gas hydrate stability zone. The second class of BSR is caused by the diagenetic transition from opal A to opal CT. The third class of BSR is always observed underneath the opal A/opal CT transition, but heat flow data and the amplitude characteristics of this arrival exclude one of the known silicate diagenetic transitions or gas hydrates as the explanation for this reflector. ODP Site 643 drilling results from the Vøring Plateau suggest two possible processes as the reason for this third BSR: (a) smectite illite conversion or (b) a sudden increase in the abundance of authigenic carbonates. The genesis of both is pressure- and temperature-dependent and could potentially result in a cross-cutting seismic reflector. The data are not conclusive as to which process is causing the third class of observed BSR.

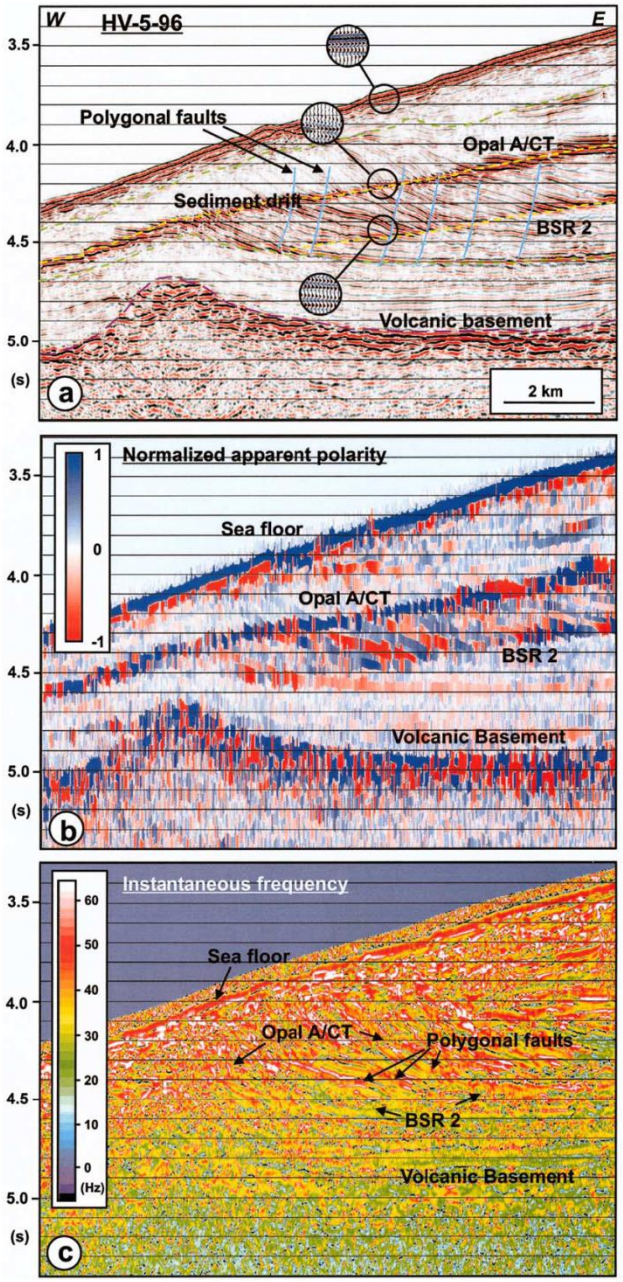

Fig. 3. Seismic-data from the western part of the Vøring Plateau showing diagenesis-related BSR related to opal A/ opal CT conversion (Fig. 1 for location). BSR 2 is a new class of bottom simulating reflectors perhaps related to smectite water expulsion. The instantaneous frequency in (c) is generally lower than in Fig. 2c because of the different seismic source.

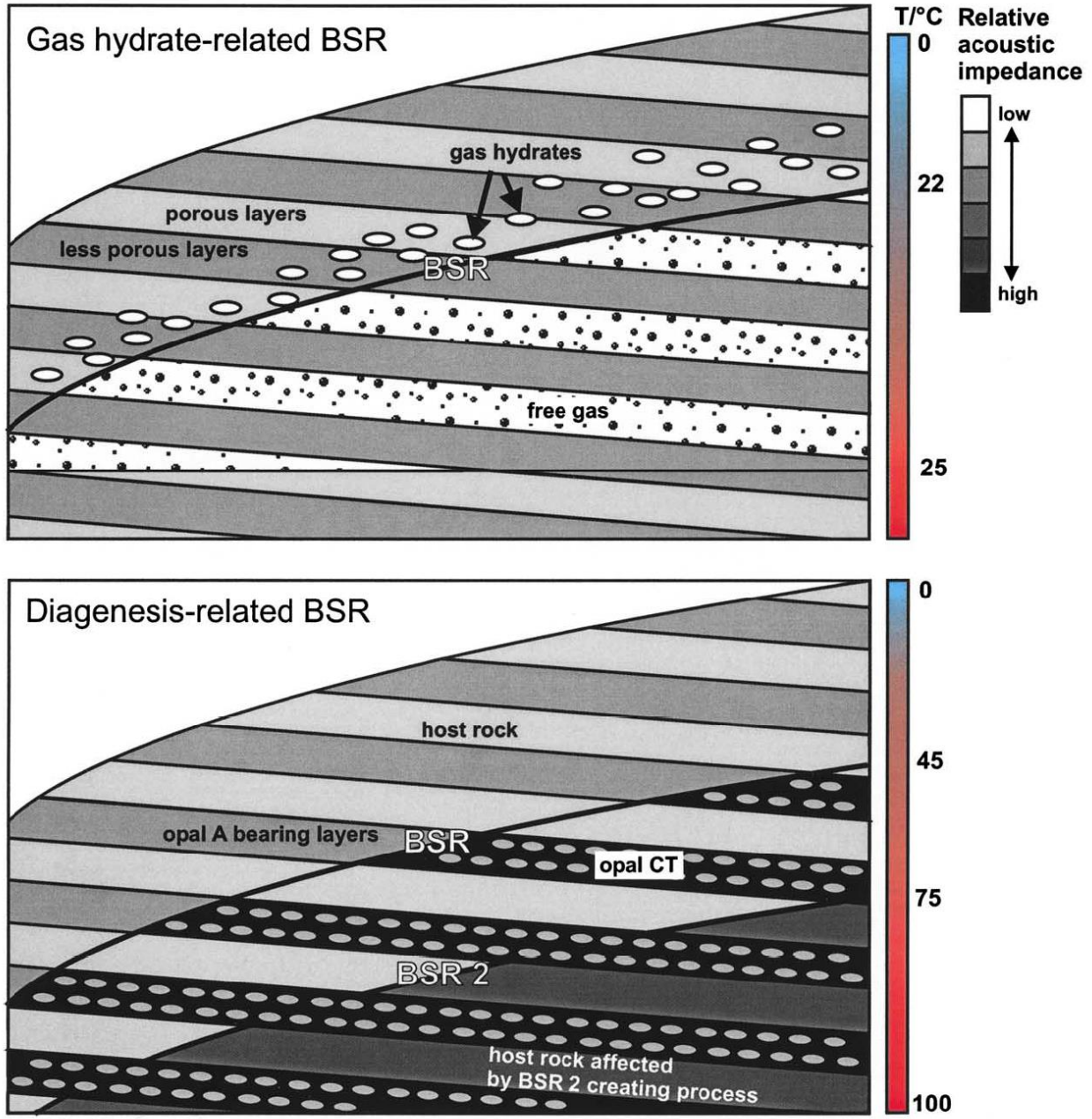

Fig. 5. Sketch outlining the changes in acoustic impedance and their causes. The temperature bars are schematic and indicate typical temperatures for the processes described in the text.